Evaluation of MEMS-Based Wireless Accelerometer Sensors in Detecting Gear Tooth Faults in Helicopter Transmissions

David G. Lewicki
Glenn Research Center
Cleveland, Ohio 44135

Nick Lambert and Robert Wagoner
Ridgetop Group Inc.
Tucson, Arizona 85741

ABSTRACT

The diagnostics capability of MEMS (micro-electro-mechanical systems) based rotating accelerometer sensors in detecting gear tooth crack failures in helicopter main-rotor transmissions was evaluated. MEMS sensors were installed on a pre-notched OH-58C spiral-bevel pinion gear. Endurance tests were performed and the gear was run to tooth fracture failure. Results from the MEMS sensor were compared to conventional accelerometers mounted on the transmission housing. Most of the four stationary accelerometers mounted on the gear box housing and most of the CI's used gave indications of failure at the end of the test. The MEMS system performed well and lasted the entire test. All MEMS accelerometers gave an indication of failure at the end of the test. The MEMS systems performed as well, if not better, than the stationary accelerometers mounted on the gear box housing with regards to gear tooth fault detection. For both the MEMS sensors and stationary sensors, the fault detection time was not much sooner than the actual tooth fracture time. The MEMS sensor spectrum data showed large first order shaft frequency sidebands due to the measurement rotating frame of reference. The method of constructing a pseudo tach signal from periodic characteristics of the vibration data was successful in deriving a TSA signal without an actual tach and proved as an effective way to improve fault detection for the MEMS.

INTRODUCTION

Gears are used extensively in rotorcraft drive systems. Effective gear fault detection is crucial to ensure flight safety. In addition, tremendous economic benefits can result from condition based maintenance practices, for which gear fault detection plays an important role. Much work has been devoted to the development of health and usage monitoring systems for rotorcraft gearbox and drivetrain components. Samuel and Pines give a comprehensive review of the state-of-the-art in vibration-based helicopter transmission diagnostics [1]. Fault detection has been documented using advanced signal processing techniques of vibration from accelerometers mounted on the transmission housing. However, for complex systems or for components buried deep in the transmission with poor signal transfer paths, alternate methods are needed to detect failures, such as embedded sensors and micro-electro-mechanical systems (MEMS) [2-7].

To improve diagnostic technology, the NASA Glenn Research Center (GRC) awarded multiple Small Business Innovation Research (SBIR) contracts to Ridgetop Group Inc. The goal was to develop prototype MEMS-based vibration sensors embedded on rotating components in a helicopter transmission. One such implementation was accelerometers embedded on a spiral-bevel pinion gear in an OH-58 helicopter main-rotor transmission. Subsequent tests were performed at GRC to evaluate fault detection capabilities.

The objective of the current study is to report the results of these tests. The diagnostics capabilities of MEMS-based, rotating accelerometer sensors in detecting gear tooth crack failures in helicopter main-rotor transmissions were evaluated and compared to those using conventional accelerometers mounted on the transmission housing. Experiments were performed on an OH-58C helicopter main-rotor transmission in the NASA GRC 500-hp helicopter transmission test facility. MEMS sensors were installed on the OH-58C spiral-bevel pinion gear. A notch was fabricated on the gear to promote gear tooth bending fatigue failure. Endurance tests were performed and the gear was run to tooth fracture failure. Results from the MEMS sensor were compared to conventional accelerometers mounted on the transmission housing.

APPARATUS

Test facility. The tests were performed in the NASA GRC 500-hp helicopter transmission test facility (Fig. 1). The test stand operates on the closed-loop or torque-regenerative principle. Mechanical power re-circulates through a closed loop of gears and shafting, part of which is the test transmission. The output of the test transmission attaches to the bevel gearbox. The output shaft of the bevel gearbox passes through a hollow shaft in the closing-end gearbox and connects to the differential gearbox. The output of the differential attaches to the hollow shaft in the closing-end gearbox. The output of the closing-end gearbox attaches to the input of the test transmission, thereby closing the loop.

A 200-hp variable-speed direct-current (DC) motor powers the test stand and controls the speed. The motor output attaches to the closing-end gearbox. The motor replenishes losses due to friction in the loop. A 15-hp DC motor provides the torque in the closed loop. This motor drives a magnetic particle clutch. The clutch output does not turn but exerts a torque. This torque is transferred through a speed reducer gearbox and a chain drive to a large sprocket on the differential gearbox. The torque on the sprocket applies torque in the closed loop by displacing the gear attached to the output shaft of the bevel gearbox with respect to the gear connected to the input shaft of the closing-end gearbox. This is done within the differential gearbox through use of a compound planetary system where the planet carrier attaches to the sprocket housing. The magnitude of torque in the loop is adjusted by changing the electric field strength of the magnetic particle clutch.

A mast shaft loading system in the test stand simulates rotor loads imposed on the OH-58C transmission output mast shaft. The OH-58C transmission output mast shaft connects to a loading yoke. Two vertical load cylinders connected to the yoke produce lift loads. A single horizontal load cylinder connected to the yoke produces a bending load. A 2000-psig nitrogen gas system powers the cylinders. Pressure regulators connected to the nitrogen supply of each of the load cylinders adjust the magnitude of lift and bending.

OH-58C test transmission. Tests were performed using an OH-58C helicopter main-rotor transmission (Fig. 2). The OH-58C transmission is rated at maximum continuous power of 335 hp at 6180 rpm input speed. The main-rotor transmission is a two-stage reduction gearbox with an overall reduction ratio of 17.44:1. The first stage is a spiral-bevel gear set with a 19-tooth pinion that meshes with a 71-tooth gear. Triplex ball bearings and one roller bearing support the bevel-pinion shaft. Duplex ball bearings and one roller bearing support the bevel-gear shaft. The pinion is straddle mounted and the gear is overhung. A planetary mesh provides the second reduction stage. The bevel-gear shaft is connected through a spline to a sun gear shaft. The 27-tooth sun gear meshes with four 35-tooth planet gears, each supported with cylindrical roller bearings. The planet gears mesh with a 99-tooth fixed ring gear. The ring gear is connected to the transmission housing through a spline on its outer diameter. Power is taken out through the planet carrier which is connected to the output mast shaft through a spline. The output shaft is supported on top by a split-inner-race ball bearing and on the bottom by a roller bearing.

The OH-58C transmission is lubricated and cooled with a dedicated lubrication system. The 71-tooth bevel gear of the first reduction stage drives a 27-tooth accessory gear. The accessory gear runs an internal oil pump, which supplies pressurized oil. After passing through the standard OH-58C 10-micron filter, the oil is ported to an external facility heater and heat exchanger, allowing precise control of oil inlet temperature. The oil is then routed back in the OH-58C transmission, providing lubrication for the gears and bearing through jets and passageways located in the transmission housing. The lubricant used in the OH-58C transmission was a synthetic base helicopter transmission oil conforming to the DOD-L-85734 specification. The nominal oil outlet pressure was 80 psig and the oil inlet pressure was 45 psig. The oil inlet temperature was 180 deg F.

The test article for this study was the spiral-bevel pinion gear. At the start of the test, a 0.01-in long x 0.03-in deep x 0.005-in wide notch was fabricated in the fillet region (loaded side) of one pinion tooth using the electric discharge machining (EDM) process. The purpose of the notch was to introduce a stress concentration in the tooth fillet and promote a bending fatigue failure of the gear tooth during prolonged running. The desired location of the notch was on the fillet radius of the tooth where a large tensile bending stress occurs during gear tooth engagement. The actual location of the notch (Fig. 3a) was a little lower than desired, biased toward the root of the gear. After 51.86 hours of run time (described later in the paper), the gear tooth did not initiate bending fatigue and the original notch was extended to 0.5-in long x 0.045-in deep x 0.005-in wide (Fig. 3b). This notch, however, was slightly misaligned to the tooth fillet and the ends of the notch were not located at the high stress regions. After 106.11 cumulative hours of run time, the gear tooth did not initiate bending fatigue and an additional notch, 0.5-in long x 0.045-in deep x 0.005-in wide, was fabricated using EDM on a second tooth (Fig. 3c). This notch was oriented in the high stress fillet region as desired, and bending fatigue occurred after 112.36 cumulative hours run time.

MEMS instrumentation. A schematic of the MEMS instrumentation setup is given in Fig. 4. For the rotating components, the accelerometer board, micro-controller board, and battery were mounted in a canister pressed into the inner bore of the OH-58C spiral-bevel pinion gear. Three MEMS accelerometers and analog-to-digital modules were installed on the accelerometer board. The micro-controller and memory chips were installed on the micro-controller board. The micro-controller transmitted and received data wirelessly to and from the stationary receiver through the transmitter antenna. The receiver transmitted data to and from the controlling laptop through use of a USB connection.

Fig. 5 shows an exploded view of the rotating MEMS instrumentation setup. As seen in the top of the figure, the accelerometer board and micro-controller board straddled the battery and were contained within the canister mounted in the spiral-bevel pinion gear. The transmitter antenna was mounted on an existing spacer ring connected to the end of the spiral-bevel pinion flange. Fig. 6 shows the MEMS receiving station. The wireless receiver was mounted close to the rotating transmitter antenna.

Fig. 7 shows a close up of the accelerometer board. Three commercially-available MEMS accelerometers were mounted on the board with specific placement and orientation. One radial accelerometer, R, was positioned at the center of the board (and center of pinion gear axis of rotation) to measure the radial (or lateral) acceleration of the pinion. Two tangential accelerometers, T1 and T2, were oriented with sensitive axes perpendicular to line T1-R-T2 to measure torsional acceleration of the pinion as well as radial acceleration. The accelerometers had a dynamic range of +/- 250 g peak acceleration, a sensitivity of 4.4 mV/g, a resonance frequency of 22 kHz, and were linear in response up to 10 kHz. The accelerometer outputs passed through a passive resistor-capacitor anti-aliasing filter circuit with an approximate cutoff frequency of approximately 15 kHz, then to commercially-available analog-to-digital converters (ADC), one for each accelerometer. The ADC's were 16-bit resolution and data were simultaneously acquired at approximately 43 kHz sample rate for one second duration. The battery chosen for the system was a 3.6-Volt DC lithium-thionyl chloride cell designed for high temperature and high power capacity. The battery life was estimated to power the MEMS system and transfer data from pinion gear to laptop at once per minute for eight hours a day for roughly one month.

Facility instrumentation. The test facility used a commercially available data acquisition system to collect and store test facility parameters. The test facility parameters were speeds, torques, oil flow rates, oil pressures, broadband vibration levels, mast loads, cycle counts, and various component temperatures. The values for each parameter were acquired, time-stamped, and stored once every second.

The NASA-developed Mechanical Diagnostics System Software (MDSS) fault detection system was used to compare with the MEMS system. The MDSS consisted of high-frequency accelerometers, shaft tachometers, and customized software equipped with gear and shaft fault detection algorithms developed throughout the years [8]. Four piezoelectric accelerometers were installed on the top-cover housing of the OH-58C transmission (Fig. 8). Two accelerometers (A1 and A2) were mounted at the input spiral-bevel pinion gear region. One (A1) was mounted in the vertical direction and the other (A2) in the horizontal direction, both to measure radial motion of the pinion shaft. Two additional accelerometers, A3 and A4, were mounted adjacent to the planetary ring gear, primarily mounted to measure ring gear radial motion. The accelerometers were commercially available and had a flat high-frequency response up to about 40 kHz and a resonant frequency of about 90 kHz. A coaxial fiber optic reflective scanner was mounted on the OH-58C transmission input shaft to produce a once-per-revolution tachometer pulse of the shaft. The outputs of the accelerometers and tachometer pulses were routed to anti-aliasing filters with a 50 kHz cut-off frequency, then to a PC-based data acquisition system. The data were acquired at 125 kHz sampling rate for one second duration.

A commercially available oil debris monitor (ODM) was also used for the tests. Pre-filtered OH-58C transmission outlet oil was routed to the ODM unit using a specially designed filter adapter block (Fig. 9). The oil was then routed back to the transmission, where it passed through the filter, and exited the transmission to the facility external heater and heat exchanger (cooler) as previously described. The output of the ODM sensor was continuously polled by the unit's conditioning box which also calculated cumulative mass of the debris as well as classifying the debris by size in predefined bin sizes. The data was routed to the MDSS monitoring PC data collection system and collected and time-stamped with the MDSS vibration data. In addition to the ODM, the standard OH-58 transmission magnetic chip detection was used. This device collects ferrous debris generated in the transmission. When excessive debris is generated, a gap in the sensor is bridged which closes an electric circuit and illuminates a warning light in the control room.

Lastly, a proximity probe was installed inside the OH-58C transmission near the spiral-bevel pinion gear using a special bracket. The probe was attached near the pinion teeth. The output of the probe conditioner was sent to an oscilloscope. This produced a sinusoidal display of the pinion teeth during rotation to visually indicate excessive movement or fracture of a tooth during test.

Test procedure. Endurance tests were performed on the OH-58C transmission spiral-bevel pinion gear. The objective was to produce a bending fatigue tooth crack on the pinion gear. Thus, the OH-58C transmission was run at constant speed and relatively high torque for many days until failure occurred. At the start of each days run, the OH-58C transmission oil was externally heated to 180 deg F. Once stabilized, the transmission input speed was set to 6180 rpm and the transmission input torque was set to either 4339 or 4649 in-lb, depending on the test. Once steady state was reached, the MDSS and MEMS systems were started. The clocks on the MDSS, MEMS, and facility data computers were all synchronized at the start of each day such that all time-stamped data were comparable to each other. The MDSS system acquired one second of data every minute. For each acquisition, the raw vibration time signals were stored as well as calculated fault condition indicators at that point in time. The MEMS system acquired one second of data continuously. At each acquisition, the raw vibration time signals for each accelerometer were transferred to the receiving station and saved on the laptop. The data transfer time from the MEMS micro-controller to the receiving station and to the laptop was dependent on receiver signal strength and slightly varied from approximately 45 to 55 seconds throughout the test. On the average, the MEMS system acquired one second of data every 51 seconds. Additional post processing of the MEMS data occurred after the tests.

RESULTS AND DISCUSSION

Test summary. Fig. 10 shows the timeline of the OH-58C endurance tests, displaying the transmission input torque versus run time for the entire test. All tests were run at full input speed of 6180 rpm. The entire test lasted 112.36 hours spanning 24 days. As previously mentioned, a 0.01-in long x 0.03-in deep x 0.005-in wide notch was fabricated in the fillet region (loaded side) of one pinion tooth at the start of the test. This condition was run for 24.59 hours at 4339 in-lb input torque (127% design). At no sign of failure, the torque was increased to 4649 in-lb (136% design). During this time, a crack occurred on the OH-58C top cover housing at 37.84 cumulative hours. This failure had no bearing on the pinion endurance tests, and a replacement cover was installed on the transmission and testing resumed. At 51.86 cumulative hours, no failure of the pinion occurred. Upon inspection, the actual location of the notch was a little lower than desired, biased toward the root of the gear. Due to this, the stress concentration on the notched pinion tooth was less than desired and no failure occurred. The original notch was extended to 0.5-in long x 0.045-in deep x 0.005-in wide. Testing resumed at 4339 in-lb input torque. At 72.51 cumulative hours, no failure occurred and the torque was increased to 4649 in-lb. During this period, indication of chips and debris were observed and testing was stopped at 106.11 cumulative hours. The transmission was disassembled, inspected, and a fatigue spall failure was discovered on the spiral-bevel gear roller bearing inner race. A replacement bearing was installed.

It was observed that the widened notch on the pinion was slightly misaligned to the tooth fillet and the ends of the notch were not located at the high stress regions. Thus, an additional notch, 0.5-in long x 0.045-in deep x 0.005-in wide, was fabricated on a second tooth. Testing resumed at 4339 in-lb input torque and increased to 4649 in-lb at 110.17 cumulative hours. At 112.30 hours, a fractured spiral-bevel pinion tooth was observed from the proximity probe data. The endurance tests concluded at 112.36 cumulative hours. The transmission was disassembled and the fractured pinion tooth occurred at the second notch location (Fig. 11), which was correctly oriented in the high fillet stress region.

MDSS results. Fig. 12 depicts the root-mean-square (RMS) of the raw vibration for the four MDSS accelerometers for the entire test. The RMS indicates the general overall vibration levels of the transmission housing. The discontinuities in the data correspond to the start and stop times for the different run days. Significant discontinuities occurred at the time of the top cover replacement (37.84 hrs) and at the time of the rebuild after the spiral-bevel gear roller bearing failure (106.11 hrs). The RMS did vary from day to day and, in general, was a poor indicator of gear tooth failure when considering data from the entire test. Fig. 13 shows the RMS for only the last 30 minutes of the last day of testing. Here, an upward trend of vibration levels can be seen at end of the test when tooth fracture occurred.

To further quantify the capabilities of the gear fault detection condition indicators (CI's) described in this paper, statistical methods will be employed. Here, the run time CI values will be compared to a running mean plus three-standard-deviation average. The CI will be defined as "fully detecting failure" if above the running average (mean plus three-standard-deviation) at the time of gear tooth failure and below the running average for the *vast majority* of time before failure (no false alarms). The CI will be defined as "marginally detecting failure" if above the running average at the time of gear tooth failure and below the running average for *most* of time before failure (some false alarms). In addition, the running mean plus three-standard-deviation average will be computed for two cases: 1) for the entire test, and 2) for only the last day of the test.

Fig. 14 shows a sample analysis using the raw RMS CI. The left column (Figs. 14a-14c) is for accelerometer A1, bevel pinion vertical. Fig. 14a shows the RMS data for the entire test along with a running mean plus three-standard-deviation average. Here, the RMS is below the running average, thus giving no indication of gear failure. Fig. 14b shows the same data for the last 30 minutes of testing, again showing no indication of failure. Fig. 14c shows the same RMS as in Fig. 14b, but with the mean plus

three-standard-deviation average calculated only for the last day of testing. Since the RMS was significantly lower the last day, the running average was also lower. However, the RMS was still lower than this running average, and thus, gave no indication of gear failure.

The right column (Figs. 14d-14e) is for accelerometer A3, ring gear. Fig. 14d shows the RMS data for the entire test along with a running mean plus three-standard-deviation average. Here, most of the RMS values were above the running average for tests after the bearing failure at 106.11 hrs, thus indicating false alarms for the majority of this data. This is further seen in Fig. 14e. The data in Fig. 14f, however, is based on a mean plus three-standard-deviation average for only the last day of testing. Here, the RMS does give an indication of gear failure at the end of the test. In summary and based on this analysis, none of the MDSS accelerometers gave an indication of gear failure using the raw RMS and a running average for the entire test. Accelerometers A2 and A3 did fully detected failure and A4 marginally detected failure when using a running average for the last day only.

Fig. 15 depicts six specific gear fault detection CI's from the MDSS system as a function of run time for the entire test. A complete definition of these CI's is given in Appendix A. The CI's were calculated from the time synchronous average (TSA) of the raw vibration data. The TSA method removes noisy data and allows the vibration signature of the gear under study to be separated from other gears or noise sources in the transmission that are non-synchronous with that gear [9]. For the OH-58C spiral-bevel pinion gear, the TSA was derived using the once-per-revolution tach pulse of the pinion gear shaft. The tach pulse was used to group vibration data in one shaft revolution increments. The groups were then resampled and time averaged to remove noise. The period of the TSA signal was one revolution of the pinion gear shaft.

RMS, sideband index (SI_1), and input shaft 3/rev of the TSA signals are shown in Figs. 15a, 15d, and 15f, respectively. FM4 and M8A of the difference signals are shown in Figs. 15b and 15e, respectively. The difference signal is the TSA signal minus the vibration at the gear mesh frequencies and first order shaft sidebands. NA4 of the residual signals is shown in Fig. 15c. The residual signal is the TSA signal minus the vibration at the gear mesh frequencies. From Fig. 15, significant discontinuities existed for RMS and SI_1, and somewhat less for NA4. Again, the discontinuities correspond to the start and stop times for the different run days. M8A was the most sensitive CI, reacting most to damage but exhibiting the most noise.

Fig. 16 shows the same CI's as in Fig. 15, but for only the last 30 minutes of run time. As stated above, pinion tooth fracture was observed at time 112.30 hours, indicated by dashed vertical lines in the figure. RMS for accelerometers A2 and A3 were fairly constant throughout the test, then increased in value at tooth fracture. This is not extremely obvious in Fig. 16a due to wide vertical-axis scaling range in order to fit the plots for all four accelerometers. Based on the statistical definitions above, the TSA RMS for A2 and A3 fully detected failure using a running average for the last day only, and marginally detected failure using a running average for the entire test (due to false alarms).

FM4 for accelerometer A3 significantly increased at the end of the test (Fig. 16b) and fully detected failure. FM4 for accelerometer A4 fully detected failure for the running average for the last day only, and marginally detected failure for the running average of the entire test. NA4 for all four accelerometers significantly increased at the end of test, fully detecting failure, and performed the best of all CI's (Fig. 16c). SI_1 for accelerometers A2 and A3 significantly increased at failure (fully detected failure), and accelerometers A1 and A4 somewhat increased at failure (Fig. 16d). M8A for accelerometer A3 significantly increased at failure (fully detected failure, Fig. 16e). Input shaft 3/rev for accelerometer A2 (Fig. 16f) increased at failure and fully detected failure using the running average of only the last day and marginally detected failure using the running average for the entire test.

Tables I and II summarize the gear fault detection capabilities for the MDSS indicators. Table I uses the running mean plus three-standard-deviation average for the entire test while Table II uses the running average for the last day only. Fault detection capability was not consistent for the four accelerometers and the seven indicators. Accelerometer A3 performed the best and all indicators gave some fault

detection (fully or marginal) with it. Accelerometer A1 performed the worst. Condition indicator NA4 performed the best and fully detected failure for all accelerometers. The fault detection capability was different when using the running average for the entire test (Table I) compared to only the last day of test (Table II). For the entire test, the standard deviation of the indicators was greater than using that for just the last day due to the increased scatter of the indicators. Thus, the criteria for fully detecting failure was more strict. As a final observation, the response from the best indicators did not react much sooner than the actual tooth fracture time (Fig. 16).

To gain insight of the MDSS vibration data, Fig. 17 shows spectra plots at two run times toward the end of the test. The first run time was at 110.50 hours (left column, Figs. 14a - 14d). This was at the start of the last day of testing. The second time was at 112.35 hours (right column, Figs. 14e - 14h) and was the last data point taken for the test, which occurred after pinion tooth fracture. All data were at 6180 rpm transmission input speed and 4649 in-lb input torque. For the test before tooth failure (left column), the majority of the vibration energy occurred at the spiral-bevel and planetary mesh fundamental and harmonic frequencies (triangles and crosses in the figures). After tooth fracture (right column), the overall energy at the spiral-bevel and planetary mesh fundamental and harmonic frequencies was similar (same vertical scale in figures between left and right columns). However, increased energy occurred at sidebands of the spiral-bevel mesh fundamental and harmonic frequencies in multiples of the transmission input shaft frequency (103 Hz). This energy is what was picked up by CI's RMS, FM4, NA4, SI_1, and M8A.

MEMS results. Fig. 18 shows the RMS of the raw broadband vibration for the MEMS sensors as a function of run time for the entire endurance test. This data was post-processed after completion of the tests. The RMS values for each of the three MEMS sensors were calculated for each one-second broadband time acquisition with DC offsets removed. Fig. 18a gives the radial accelerometer, R, Fig. 18b gives the tangential accelerometer, T1, and Fig. 18c gives the tangential accelerometer, T2 (refer to Fig. 7) plotted versus cumulative run time. The radial accelerometer measured radial or lateral motion of the pinion gear shaft. The tangential accelerometers measured radial motion as well as tangential or rotational acceleration of the gear shaft. Adding the signals of the tangential accelerometers (T1+T2, Fig. 18d) results in purely torsional motion since the T1 and T2 accelerometers are positioned at opposite polarity (Fig. 7). Subtracting the signals of the tangential accelerometers (T1-T2, Fig. 18e) results in just radial motion and is similar to the radial accelerometer, R.

Overall, the MEMS system performed well and lasted the entire 112.36-hour test. At 11.50 hours cumulative run time, the MEMS battery, accelerometer board, and transmitter board were replaced with spare units. This was due to difficulties encountered with the sleep portion of the controlling software, which would reduce battery power during non-run time. At 51.86 hours run time, the battery and transmitter board were replaced with additional spare units. This was due to a long period of inactivity in which an additional notch was being fabricated on the test pinion gear.

Fig. 19 shows the same data as Fig. 18, but expanded for only the last 30 minutes of test. From the RMS, all three accelerometers (R, T1, and T2) gave an indication of failure at the end of the test (Figs. 19a, 19b, and 19c). Based on the statistical definition previously defines, accelerometers R and T2 fully detected failure and accelerometer marginally detected failure using the running average for the entire test and all accelerometers fully detected failure using the running average of only the last day. As with the MDSS data, the MEMS sensors did not respond much sooner than the actual tooth fracture time.

To gain insight of the MEMS vibration data, Fig. 20 shows spectra plots at two run times toward the end of the test. The first run time was at 110.49 hours (left column, Figs. 20a - 20e). This was at the start of the last day of testing. The second time was at 112.35 hours (right column, Figs. 20f - 20j) and was the last data point taken for the test, which occurred after pinion tooth fracture. All data were at 6180 rpm transmission input speed and 4649 in-lb input torque.

For the radial accelerometer, only radial or lateral motion is measured. The measurement direction of the sensor rotates in a sinusoidal manor with the pinion gear shaft. Thus, the measured response from the radial accelerometer is the product of a sinusoidal function of the pinion shaft frequency and a sinusoidal function of the radial motion, such as from the gear mesh frequencies. The product of trigonometric functions is given by [10]

$$\cos A \cos B = 0.5 \{ \cos(A - B) + \cos(A + B) \} \tag{1}$$

$$\sin A \sin B = 0.5 \{ \cos(A - B) - \cos(A + B) \} \tag{2}$$

Thus, the vibration for the spiral-bevel gear mesh will not occur at the mesh frequencies, f_m, but at the sideband frequencies f_m+f_s and f_m-f_s, where f_s is the shaft frequency. The spectrum for the radial accelerometer in Fig. 20a illustrates this phenomenon. Vibration did not occur at the spiral-bevel mesh frequencies, 1957 (meshing frequency), 3914 (1st harmonic), and 5871 (2nd harmonic) Hz. They occurred at $1957 \pm 103 = 1854$ and 2060 Hz (meshing frequencies), $3914 \pm 103 = 3811$ and 4017 Hz (1st harmonic), and $5871 \pm 103 = 5768$ and 5974 Hz (2nd harmonic), where the shaft frequency was 103 Hz.

For the tangential accelerometers, radial motion and tangential motion are measured. The torsional motion will cause vibration directly at the gear meshing frequencies since this motion follows the rotating measurement position. The radial motion will cause the sidebands as described above. Figs. 20b and 20c show this where vibration spikes occur at 3811, 3914, 4017, 5768, 5871, and 5974 Hz for the spiral-bevel mesh second and third harmonic frequencies. It is interesting to note that there is no torsional vibration at the spiral-bevel meshing frequency of 1957 Hz. Accelerometers T1 and T2 gave very similar responses. Fig. 20d depicts the vibration from T1+T2, which is the torsional acceleration. Here, the radial/lateral portion is cancelled out, and thus, vibration occurred at the gear meshing frequencies and not the sidebands as in R, T1, and T2. Fig. 20e shows the vibration from T1-T2. Here, the torsional portion is cancelled out and the response is similar to the radial accelerometer from Fig. 20a.

For the data before tooth failure (Fig. 20 left column), the majority of the vibration energy occurred at the spiral-bevel mesh, harmonic, and sideband frequencies (triangles in the figures). Only a small amount of energy occurred at the planetary mesh frequencies (cross in figures) since the MEMS sensing package was installed directly on the rotating spiral-bevel pinion gear shaft. After tooth fracture (right column), the overall energy at the spiral-bevel and planetary mesh fundamental and harmonic frequencies was similar (same vertical scale in figures between left and right columns). However, much increased energy occurred through the complete spectrum, with an emphasis on sidebands at multiples of the bevel gear shaft frequency. This was the reason the RMS indicator on the overall broadband signal did detect tooth failure.

It was desired to apply time synchronous averaging to the MEMS data to investigate if it improved fault detectability. There was, however, no tach pulse associated with the saved MEMS data. The method of Bechhoefer [11] was used to construct a pseudo tach signal from the periodic characteristics of the vibration data. From this method, the vibration time signal was filtered around a strong periodic signal with high signal-to-noise ratio, such as a gear mesh fundamental or harmonic frequency, using a narrow band pass filter. The filtered signal was fed to a zero-crossings algorithm which calculated the time and index when the signal crossed zero in a positive sense. The resulting indexes were used to determine the gear shaft period. As an example, every 3 x 19 = 57 indexes from the zero-crossings routine would indicate one rotation of the gear shaft if the 3rd harmonic frequency of a 19-tooth gear was used for the pass band frequency.

First, this method was applied to MDSS data to compare the TSA calculated from the pseudo tach signal to that calculated from the actual tach signal. Fig. 21a shows a sample spectrum from MDSS accelerometer A2 at run time 110.50 hours (same data as in Fig. 17b). The black data is the spectrum

from the raw time signal and the red data is the spectrum from the filtered signal used for the pseudo tach calculation. The red data was filtered around 5872 Hz, which was the 3rd harmonic of the spiral-bevel mesh. Fig. 21b shows the calculated pseudo tach from the zero-crossings routine. The mean calculated speed from the pseudo tach data was 6182 rpm, which correlated exactly with that from the facility data acquisition speed sensor. Fig. 21c compares the TSA's. The black data is the MDSS-calculated TSA using the measured tach signal. The red data is the TSA using the pseudo tach signal. As seen in the figure, good correlation between the TSA using the measured tach signal to that using the pseudo tach signal is seen.

Fig. 22 shows a sample TSA from the MEMS data at run time 110.49 hours. Tangential accelerometer T1 was used to extract the pseudo tach signal and Fig. 22a shows the spectrum. The filtered data around 3915 Hz (spiral-bevel mesh 2nd harmonic frequency) was used because it was the cleanest gear harmonic. Figs. 22b through 22d depict the TSA's for accelerometers R, T1, and T2, respectively. Figs. 22e through 22g shows the spectrums of the TSA's. For this example, a relatively large once-per-revolution oscillation occurred. The period of the TSA signal was one gear shaft rotation. A total of 512 interpolated point were used for the TSA. This gave a bandwidth of one shaft order (103 Hz) in the frequency domain. As expected, energy is seen around the spiral-bevel gear mesh fundamental and harmonics frequencies, with higher activity at the 2nd and 3rd harmonics. Similar results were obtained when accelerometer T2 was used to extract the pseudo tach signal. Radial accelerometer R could not be used to extract the pseudo tach signal since it did not exhibit strong energy directly at any gear mesh harmonic frequency.

Fig. 23 shows six gear fault detection CI's calculated from the pseudo tach TSA signals of the MEMS data. The CI's are shown as a function of run time for the entire test. These CI's can be compared to those from the MDSS (Fig. 15). Note that SI_3 performed better than SI_1 for the MEMS data and is shown in the results. In general, the MEMS CI's were a little noisier than those from the MDSS, but all exhibited an increase in value at gear tooth failure at the end of the test. Fig. 24 shows the MEMS CI's for the last 30 minutes of the testing. Again, gear tooth failure occurred at 112.30 hrs. Tables III and IV summarize the gear fault detection capabilities for the MEMS indicators. Table III uses the running mean plus three-standard-deviation average for the entire test while Table IV uses the running average for the last day only. All CI's for all accelerometers give an indication of failure when using the running average of only the last day (Table IV). Raw RMS, TSA RMS, NA4, and SI_3 fully detected failure for all accelerometers. Accelerometer T1 performed the best where all CI's fully detected failure. This was probably due to accelerometer T1 being physically closest to the fractured gear tooth (Fig. 7). The method of constructing a pseudo tach signal from periodic characteristics of the vibration data was successful in deriving a TSA signal without an actual tach and proved as an effective way to improve fault detection. As with the MDSS results, the fault detection capability was rated lower when the running average used data from the entire test (Table III) due to increased scatter. The MEMS CI's reacted to the gear failure at a similar time as that from the MDSS data, again, not much sooner than the actual tooth fracture. In comparing the gear fault detection capability of the MDSS to the MEMS (comparing Tables I through IV), the MEMS systems performed as well, if not better, than the MDSS.

Bearing failure detection. As previously mentioned, a fatigue spall failure was discovered on the spiral-bevel gear roller bearing inner race at 106.11 hours run time. Fig. 25a shows the cumulative mass of the oil debris sensor as a function of run time for the entire test. From 0 to 9 hours, the debris increased from 0 to 29 mg, exhibiting a common "cleaning" condition. From the 29 to 58 hours, discrete increases in debris were measured. At 58 hours, the measured debris rapidly increased with time, giving a pronounced indication of component failure. At 59 hours, the OH-58 transmission flight hardware chip detector started to give indication of debris also. The transmission was disassembled and inspected at 106.11 hours run time, and the spalled spiral-bevel gear roller bearing inner race was discovered.

Fig. 25b shows the processed vibration data from MDSS accelerometer A3. This data used a common method for rolling element bearing fault detection in which the raw data was band pass filtered and

enveloped [12]. Shown in the figure are the magnitudes of the inner race bearing frequency of filtered and enveloped data. Some disturbance is shown at about 70 hours, but significant response to the fault is shown at about 86 hours. This analysis used band pass frequencies from 30 to 50 kHz. Fault detection was possibly in this range since high-frequency energy from the bearing was measured using the MDSS high-frequency accelerometers while low-frequency noise from the gear mesh was filtered and removed. Subsequent analysis was performed using lower band pass frequencies. Bearing failure was not detected, however, for lower limit band pass frequencies less than 30 kHz.

The MEMS vibration data did not give any indication of the bearing failure. This was most likely due to the limited frequency content of the sensors. The system was designed to detect spiral-bevel pinion gear failure, and was limited to around 44 kHz sampling rate, and thus, 22 kHz maximum usable frequency. As stated above, the MDSS needed 30 to 50 kHz band pass filters to detect bearing failure.

CONCLUSIONS

The diagnostics capability of MEMS-based, rotating accelerometer sensors in detecting gear tooth crack failures in helicopter main-rotor transmissions was evaluated. MEMS sensors were installed on a pre-notched spiral-bevel pinion gear inside the OH-58C helicopter main-rotor transmission. Endurance tests were performed and the gear was run to tooth fracture failure. Results from the MEMS sensor were compared to conventional accelerometers mounted on the transmission housing. The following results were obtained:

1) The MEMS system performed well and lasted the entire 112.36-hour test, providing both rotational vibration and speed measurement data.

2) All three MEMS accelerometers mounted inside the gear box gave an indication of failure at the end of the test.

3) Most of the four stationary accelerometers mounted on the gear box housing and most of the CI's used gave indications of failure at the end of the test.

4) The MEMS systems performed as well, if not better, than the stationary accelerometers mounted on the gear box housing with regards to gear tooth fault detection.

5) For both the MEMS sensors and stationary sensors, the fault detection time was not much sooner than the actual tooth fracture time.

6) The MEMS sensor spectrum data showed large first order shaft frequency sidebands due to the measurement rotating frame of reference.

7) The method of constructing a pseudo tach signal from periodic characteristics of the vibration data was successful in deriving a TSA signal without an actual tach and proved as an effective way to improve fault detection for the MEMS data.

REFERENCES

1. Samuel, P.D., and Pines, D.J., "A Review of Vibration-Based Techniques for Helicopter Transmission Diagnostics", Journal of Sound and Vibration, Vol. 282, No. 1-2, pp. 475-508, 2005.

2. Suryavanashi, A., Wang, S., Gao, R., Danai, K., and Lewicki, D., "Condition Monitoring of Helicopter Gearboxes by Embedding Sensing", Proceedings of American Helicopter Society 58th Annual Forum, Montreal, Quebec, Canada, June 11-13, 2002.

3. Ghoshal, A., Welsh, G.S., Gurvich, M.R., Butler, S.L., Winston, H., Costiner, S., Attridge, P., Urban, M.R., and Bordick, N., "Smart Embedded Sensors in Rotorcraft Composite Components for Condition Based Maintenance", Proceedings of the American Helicopter Society 66th Annual Forum, Phoenix, AZ, May 11-13, 2010.

4. Baldwin, C.S., Kiddy, J.S., and Samuel, P.D., "Towards Development of a Fiber Optic-Based Transmission Monitoring System", Proceedings of SPIE Vol. 8026 Photonic Applications for Aerospace, Transportation, and Harsh Environment II, Orlando, FL, May 25, 2011.

5. Berdy, D., Adams, D., Jang, J.H., Jung, B., Peroulis, D., Sadeghi, F., and Scott, S., "Self-Powered Helicopter Health Monitoring Sensor", Proceedings of the American Helicopter Society 66th Annual Forum, Phoenix, AZ, May 11-13, 2010.

6. Scott, S.; Kovacs, A.; Gupta, L.; Katz, J.; Sadeghi, F.; Peroulis, D., "Wireless Temperature Microsensors Integrated on Bearings for Health Monitoring Applications", Proceedings of the 24th IEEE International Conference on Micro Electro Mechanical Systems, Jan. 23-27, 2011.

7. Qin, G. Hu, N., "Design of Embedded Wireless Sensor and Its Soft Encapsulation for Embedded Monitoring of Helicopter Planetary Gear Set", Proceedings of the 25th International Congress on Condition Monitoring and Diagnostic Engineering, Journal of Physics: Conference Series 364, 2012.

8. Dempsey, P.J., "Data Fusion Tool for Spiral Bevel Gear Condition Indicator Data", Proceedings of the Society for Machinery Failure Prevention Technology for the Society's 68th Conference, May 20-22, 2014.

9. Stewart, R.M., "Some Useful Data Analysis Techniques for Gearbox Diagnostics", Report MHM/R/10/77, Machine Health Monitoring Group, Institute of Sound and Vibration Research, University of Southampton, Jul. 1977.

10. Spiegel, M.R., "Mathematical Handbook, Schaum's Outline Series", McGraw-Hill Book Company, 1968.

11. Bechhoefer, E., and Kingsley, M., "A Review of Time Synchronous Average Algorithms", Proceedings of the Annual Conference of the Prognostics and Health Management Society, San Diego, CA, Sep. 27 – Oct. 1, 2009.

12. Randall, R.B., Antoni, J., "Rolling Element Bearing Diagnostics - A Tutorial", Mechanical Systems and Signal Processing, Vol. 25, pp. 485–520, 2011.

13. Zakrajsek, J.J., Townsend, D.P., and Decker, H.J., "An Analysis of Gear Fault Detection Methods as Applied to Pitting Fatigue Failure Data", Proceedings of the Machinery Failure Prevention Technology for the Society's 47th Conference, Apr. 13-15, 1993.

14. Martin, H.R., "Statistical Moment Analysis as a Means of Surface Damage Detection", Proceedings of the Seventh International Modal Analysis Conference, Society for Experimental Mechanics, Schenectady, NY, 1989, pp. 1016–1021.

15. Antolick, L.J, Branning, J.S., Wade, D.R., and Dempsey, P.J., "Evaluation of Gear Condition Indicator Performance on Rotorcraft Fleet", Proceedings of the American Helicopter Society 66th Annual Forum, Phoenix, AZ, May 11-13, 2010.

16. Lewicki, D.G., Heath, G.F., Filler, R.R., Slaughter, S.C., and Fetty, J., "Face-Gear Surface Durability Investigations", Journal of the American Helicopter Society, Vol. 53, No. 3, pp. 282-289, Jul. 2008.

APPENDIX A - CONDITION INDICATOR (CI) DEFINITIONS

Root Mean Square. The root mean square (RMS) is defined as the square root of the average of the sum of the squares of the TSA vibration signal (Eqn. A1). For a simple sine wave vibration trace, the RMS value is approximately 0.707 times the amplitude of the signal.

$$RMS = \sqrt{\frac{1}{N}\left[\sum_{i=1}^{N} S_i^2\right]}$$
(A1)

where

S time-synchronous-averaged (TSA) vibration trace
i data point number in vibration trace
N total number of data points in vibration trace

FM4. The FM4 parameter (Eqn. A2) was developed to detect changes in vibration pattern resulting from damage to a single gear tooth [9]. The metric is calculated by dividing the fourth statistical moment (kurtosis) of the difference signal by the square of the variance of the difference signal. The difference signal is defined as the time-averaged vibration trace, S, minus the vibration at the gear mesh frequencies and first order shaft sidebands. The metric is non-dimensional with a nominal value of 3 for Gaussian noise (assumed for a healthy component).

$$FM4 = \frac{N \sum_{i=1}^{N}\left(d_i - \bar{d}\right)^4}{\left[\sum_{i=1}^{N}\left(d_i - \bar{d}\right)^2\right]^2}$$
(A2)

where

d difference signal
$\bar{d}$ mean value of difference signal
i data point number in difference signal
N total number of data points in difference signal

NA4. The NA4 metric (Eqn. A3) was developed to overcome a shortcoming of the FM4 metric [13]. As the occurrences of damage progresses in both number and severity, FM4 becomes less sensitive to the new damage. Two changes were made to the FM4 metric to develop the NA4 metric as one that is more sensitive to progressing damage. One change is that FM4 is calculated from the difference signal while NA4 is calculated from the residual signal. The residual signal includes the first order gear sidebands that were removed from the difference signal. The second change is that trending was incorporated into the NA4 metric. While FM4 is calculated as the ratio of the kurtosis of the data record divided by the square of the variance of the same data record, NA4 is calculated as the ratio of the kurtosis of the data record divided by the square of the average variance. The average variance is the mean value of the variance of all previous data records in the run ensemble. These two changes make the NA4 metric a more sensitive and robust metric. The NA4 metric is calculated by

$$NA4 = \frac{N \sum_{i=1}^{N}(r_i - \bar{r})^4}{\left[\frac{1}{M}\sum_{j=1}^{M}\sum_{i=1}^{N}\left(r_{ij} - \bar{r}\right)^2\right]^2}$$
(A3)

where

r	residual signal
$\bar{r}$	mean value of residual signal
i	data point number in residual signal
N	total number of points in residual signal
j	time record number in run ensemble
M	current time record in run ensemble

M8A. The parameter M8A was proposed by Martin [14] and was designed to be more sensitive than FM4 or NA4 to peaks in the difference signal. M8A uses the eight moment normalized by the variance to the fourth power and is given as

$$M8A = \frac{N^3 \; \sum_{i=1}^{N}(d_i - \bar{d})^8}{\left[\sum_{i=1}^{N}(d_i - \bar{d})^2\right]^4} \tag{A4}$$

SI. The sideband index, SI_1, is a measure of local gear faults and is defined as the average of the first shaft order sidebands of the gear mesh fundamental frequency [15]. An increase in magnitude of the sidebands drives this CI and indicates a local fault, and is given by

$$SI_1 = \frac{y_{-1} + y_{+1}}{2} \tag{A5}$$

where

y_{-1}	magnitude of TSA spectrum at frequency (f_m -f_s), where f_m = gear mesh fundamental frequency and f_s = gear shaft frequency
y_{+1}	magnitude of TSA spectrum at frequency (f_m +f_s)

A slight deviation of this parameter is to use the first three sideband about the gear mesh frequency where

$$SI_3 = \frac{y_{-3} + y_{-2} + y_{-1} + y_{+1} + y_{+2} + y_{+3}}{6} \tag{A6}$$

where

$y_{\pm i}$	magnitude of TSA spectrum at frequency ($f_m \pm i f_s$, i=1 to 3)

Input shaft 3/rev. The input shaft 3/rev parameter is the magnitude of the TSA spectrum at a frequency of three time the shaft speed. From previous gear endurance tests [16], it was shown that a gear fault disturbed the simply once per revolution periodicity of the TSA signal. The magnitude at two to ten shaft orders were increased for a local gear fault. Trending the three per revolution magnitude was effective in detecting gear tooth local failures.

Table I. Gear tooth fault detection capability, MDSS data.
(Mean plus three-standard deviation running average based on entire test).

Condition indicator	Accelerometer			
	A1	A2	A3	A4
RMS (raw)				
RMS (TSA)		m	m	
FM4		m	**Y**	m
NA4	**Y**	**Y**	**Y**	**Y**
SI$_1$, g		**Y**	**Y**	
M8A		m	**Y**	m
Input Shaft 3/rev, g		m		

Y, Failure fully detected
m, Failure marginally detected

Table II. Gear tooth fault detection capability, MDSS data.
(Mean plus three-standard deviation running average based on last day of test).

Condition indicator	Accelerometer			
	A1	A2	A3	A4
RMS (raw)		**Y**	**Y**	m
RMS (TSA)	**Y**	**Y**	**Y**	**Y**
FM4		m	**Y**	**Y**
NA4	**Y**	**Y**	**Y**	**Y**
SI$_1$, g	m	**Y**	**Y**	**Y**
M8A			**Y**	**Y**
Input Shaft 3/rev, g	m	**Y**		

Table III. Gear tooth fault detection capability, MEMS data.
(Mean plus three-standard deviation running average based on entire test).

Condition indicator	Accelerometer		
	R	T1	T2
RMS (raw)	**Y**	m	**Y**
RMS (TSA)	**Y**	m	m
FM4		m	m
NA4	m	m	m
SI$_3$, g	**Y**		
M8A		m	m
Input Shaft 3/rev, g	m	m	m

Table IV. Gear tooth fault detection capability, MEMS data.
(Mean plus three-standard deviation running average based on last day of test).

Condition indicator	Accelerometer		
	R	T1	T2
RMS (raw)	**Y**	**Y**	**Y**
RMS (TSA)	**Y**	**Y**	**Y**
FM4	m	**Y**	m
NA4	**Y**	**Y**	**Y**
SI_3, g	**Y**	**Y**	**Y**
M8A	m	**Y**	m
Input Shaft 3/rev, g	**Y**	**Y**	m
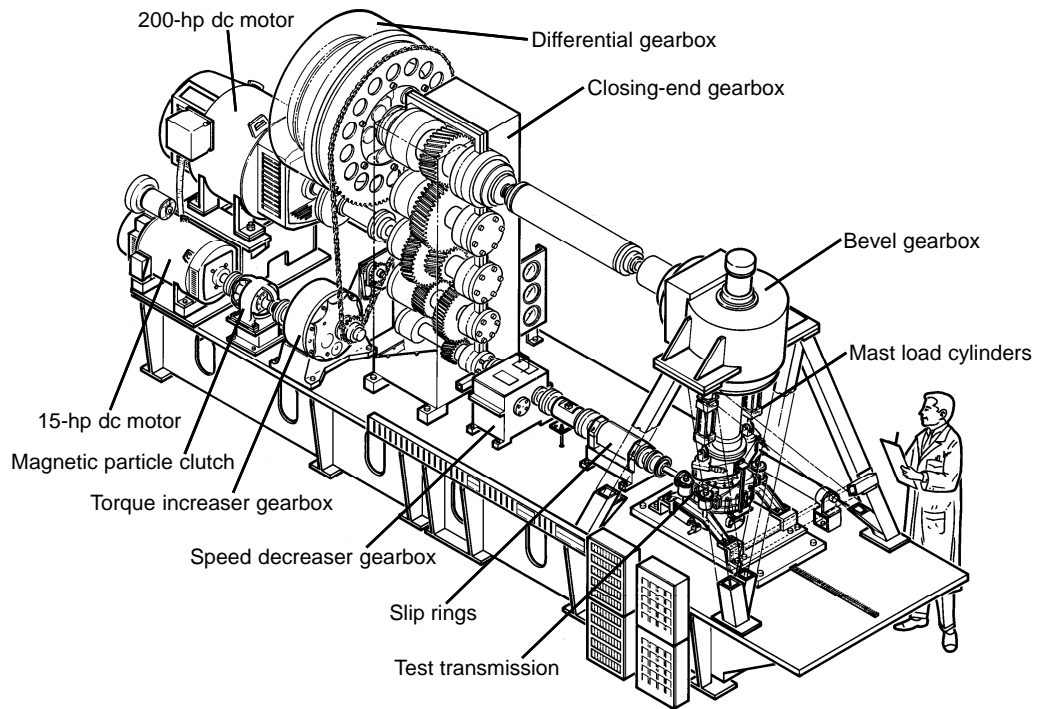
Fig. 1. NASA Glenn 500-hp helicopter transmission test facility.
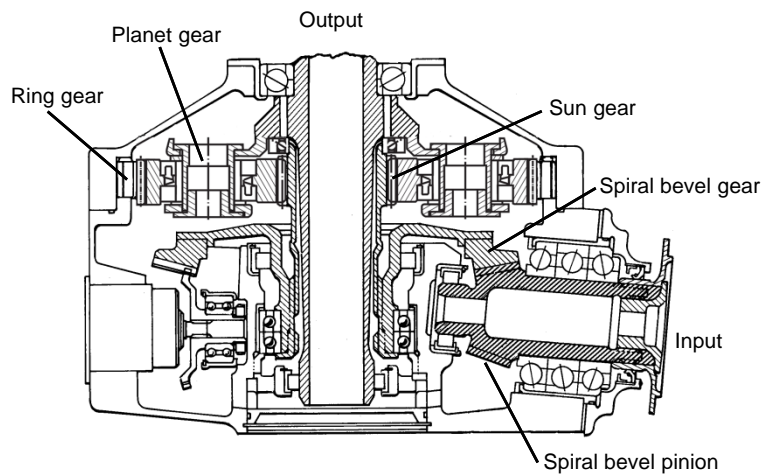
Fig. 2. OH-58C helicopter main-rotor transmission.
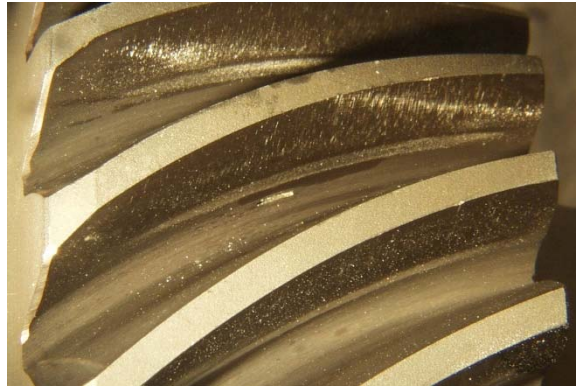
a) Original notch, inserted at run time = 0 hrs.
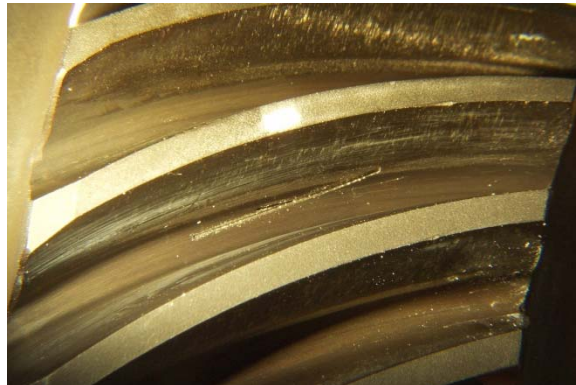
b) Extended notch , inserted at run time = 51.86 hrs.
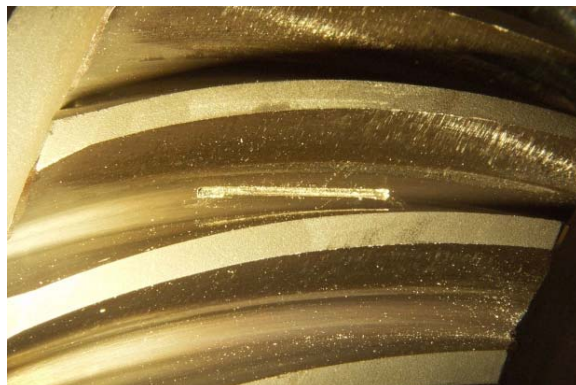
c) Additional notch , inserted at run time = 106.11 hrs.

Fig. 3. Fabricated notches on OH-58C spiral-bevel pinion gear teeth.

Fig. 4. MEMS instrumentation setup.

Micro-controller board   Accelerometer board   Canister

Battery

MEMS Sensing Package

MEMS transmitter antenna

OH-58C
pinion gear

Input
shaft
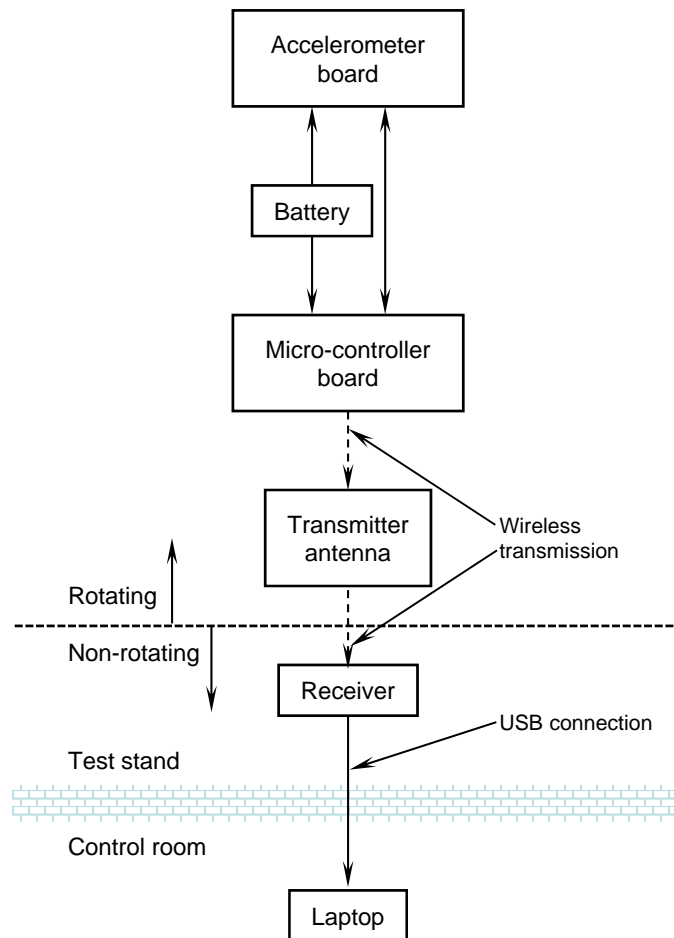
OH-58C transmission
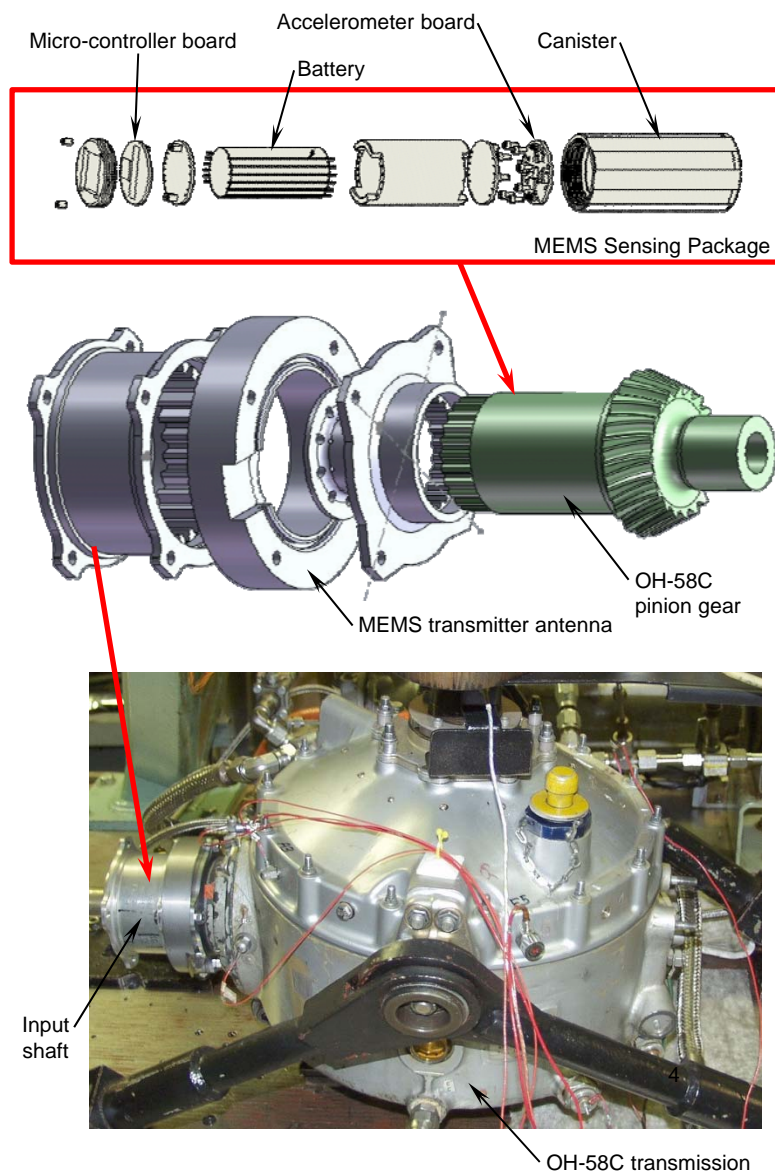
Fig. 5. MEMS sensing package and installation in OH-58C transmission.
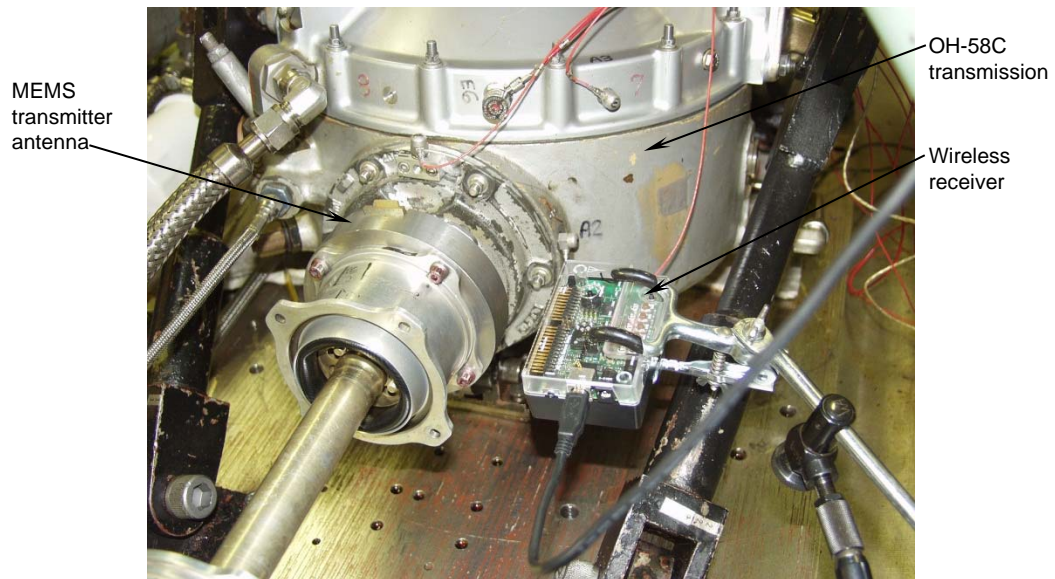
Fig. 6. MEMS receiving station.
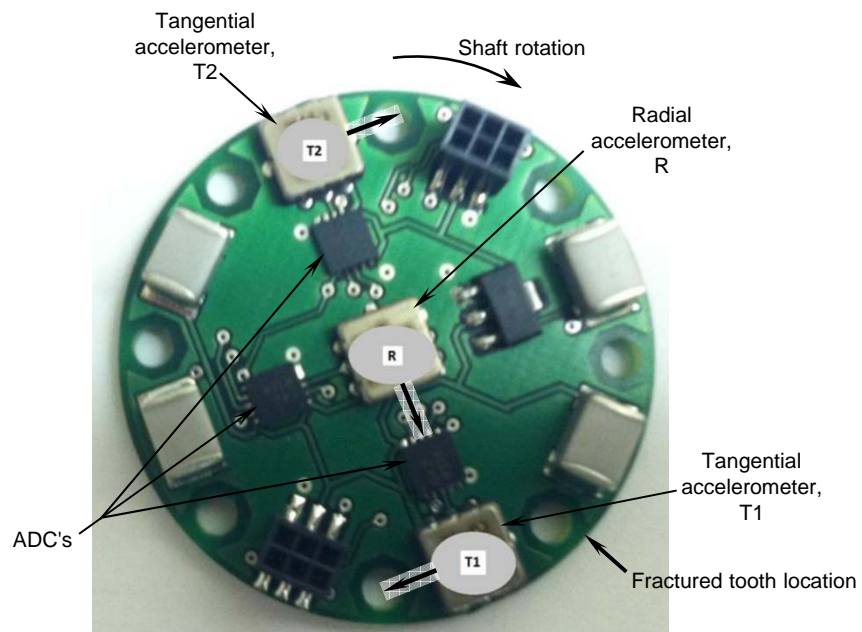
Fig. 7. MEMS accelerometer board.

a) Top view.

A3

A2

A4

Tach pulse, input shaft

A1

b) Side view.
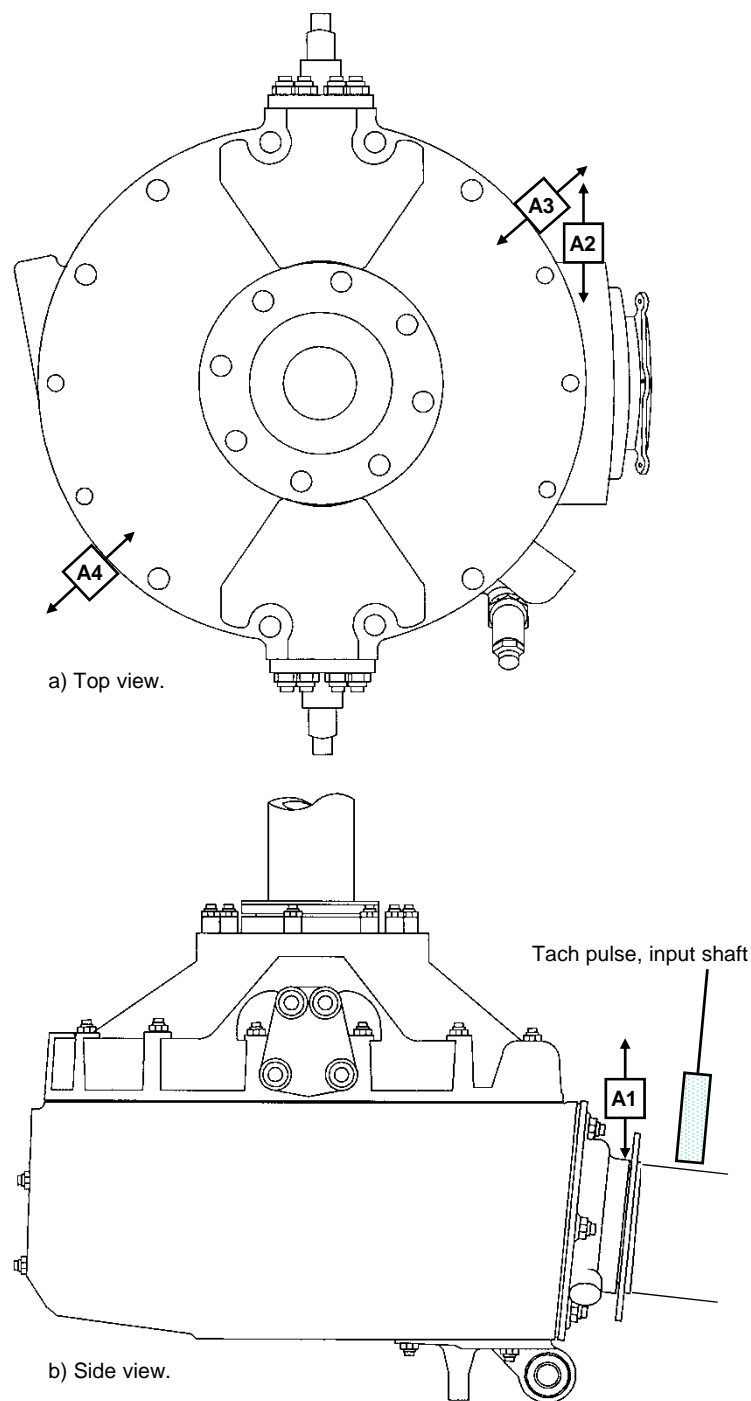
Fig. 8. Accelerometer locations on OH-58C transmission top cover housing.

OH-58C transmission

Pre-filter oil outlet adapter block

OH-58 transmission oil filter

Filter oil outlet, to heater & cooler

Pre-filtered oil flow

Oil debris monitoring (ODM) sensor

ODM controller

Test stand

Control room

Serial port

Data acquisition PC
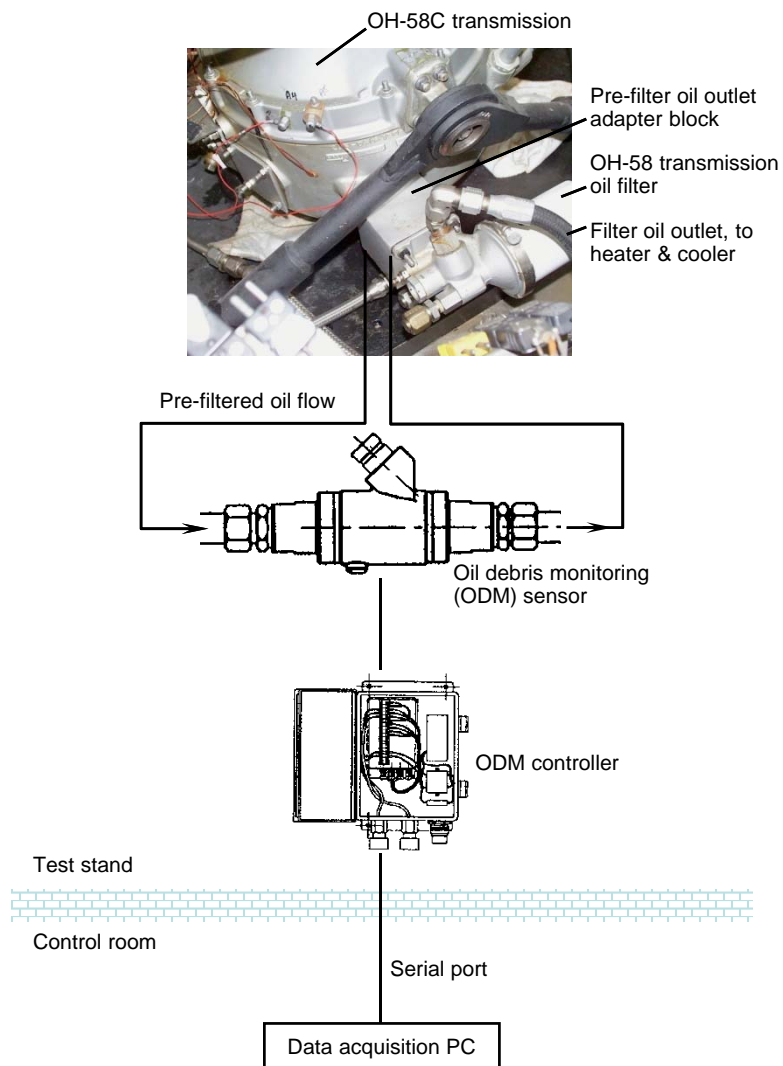
Fig. 9. Oil debris monitoring setup.
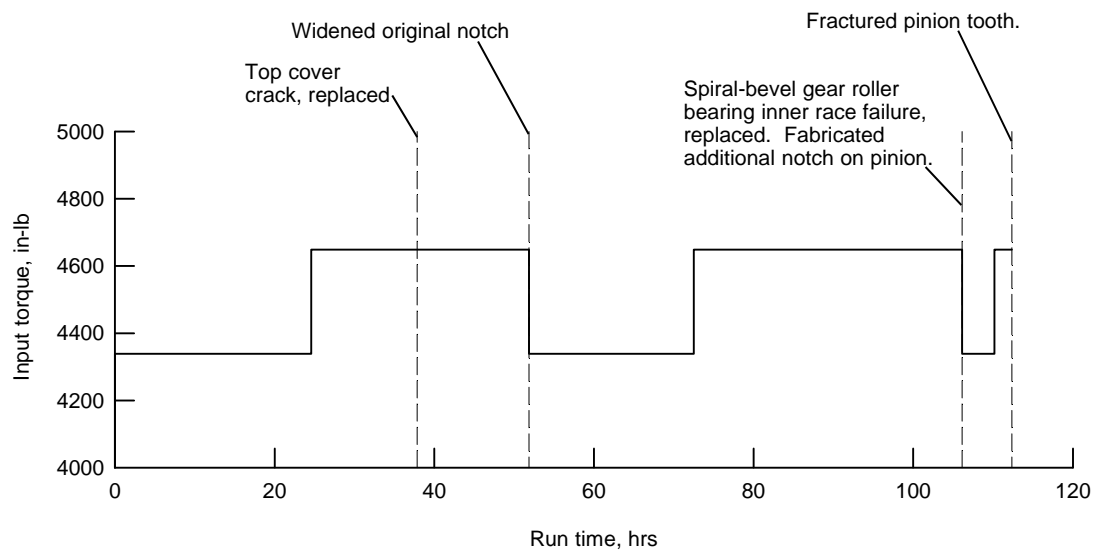
Fig. 10. Timeline of spiral-bevel pinion endurance tests.

Fig. 11. Fractured spiral-bevel pinion tooth after 112.36 hrs run time.
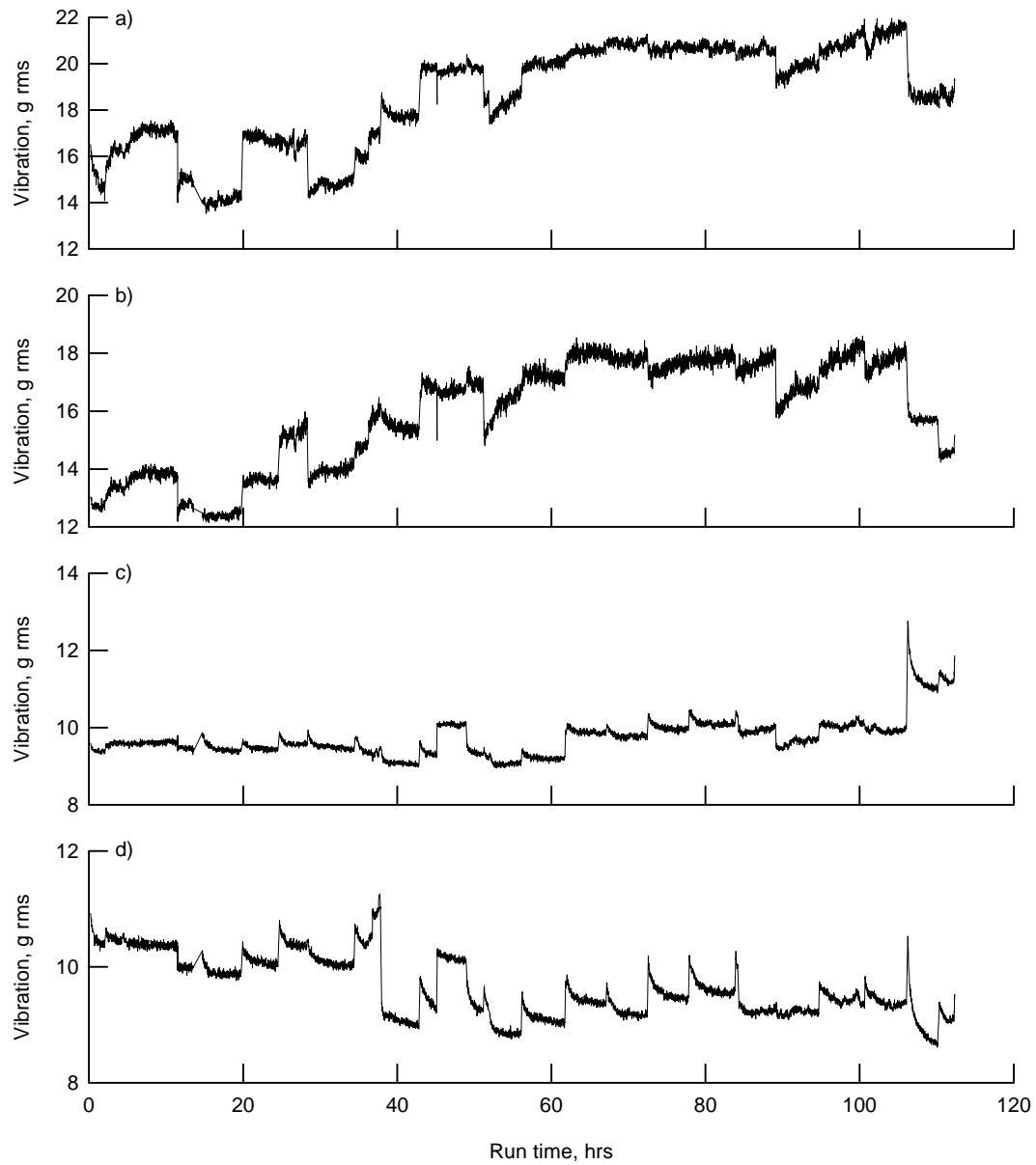
Fig. 12. RMS of MDSS raw vibration for entire test. a) Accelerometer A1, bevel pinion vertical. b) Accelerometer A2, bevel pinion horizontal. c) Accelerometer A3, ring gear. d) Accelerometer A4, ring gear.
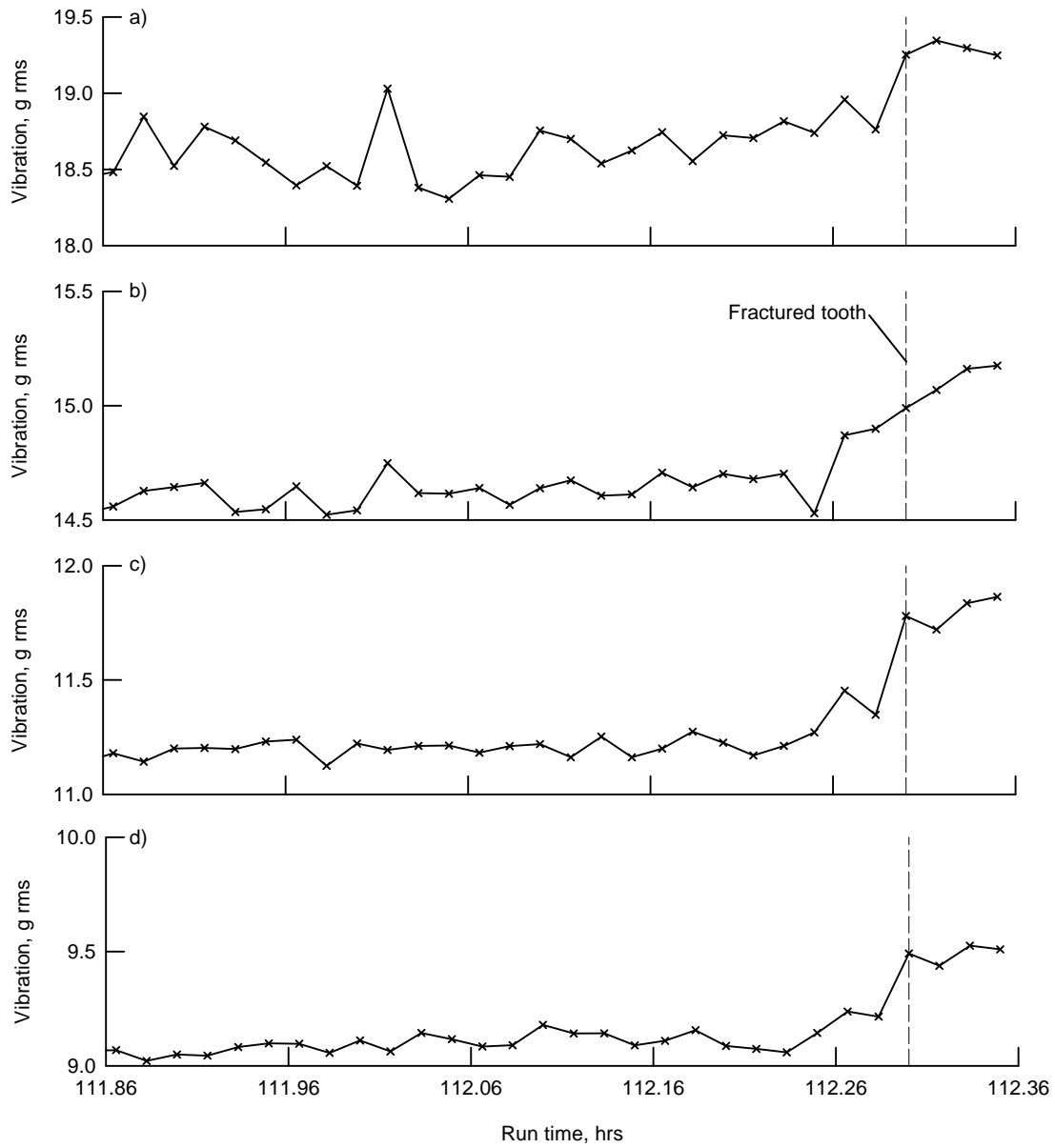
Fig. 13. RMS of MDSS raw vibration for last 30 minutes of test. a) Accelerometer A1, bevel pinion vertical.
b) Accelerometer A2, bevel pinion horizontal. c) Accelerometer A3, ring gear. d) Accelerometer A4, ring gear.
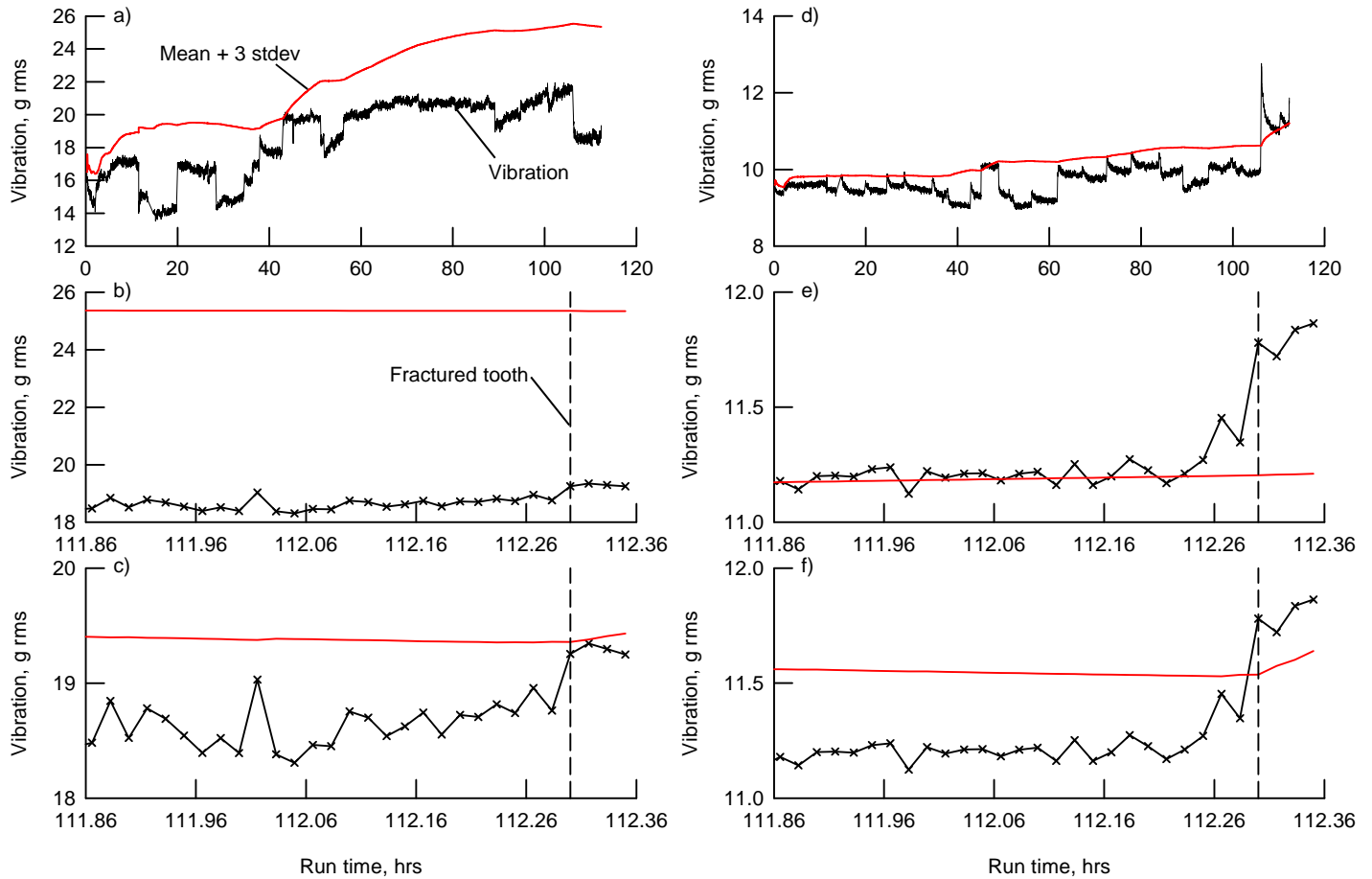
Fig. 14. Evaluation of fault detection capability, RMS of MDSS raw vibration.
a) Accelerometer A1, entire test.
b) Accelerometer A1, last 30 minutes of test.
c) Accelerometer A1, last 30 minutes of test, mean and standard deviation
   evaluated for last day of test only.
d) Accelerometer A3, entire test.
e) Accelerometer A3, last 30 minutes of test.
f) Accelerometer A3, last 30 minutes of test, mean and standard deviation
   evaluated for last day of test only.
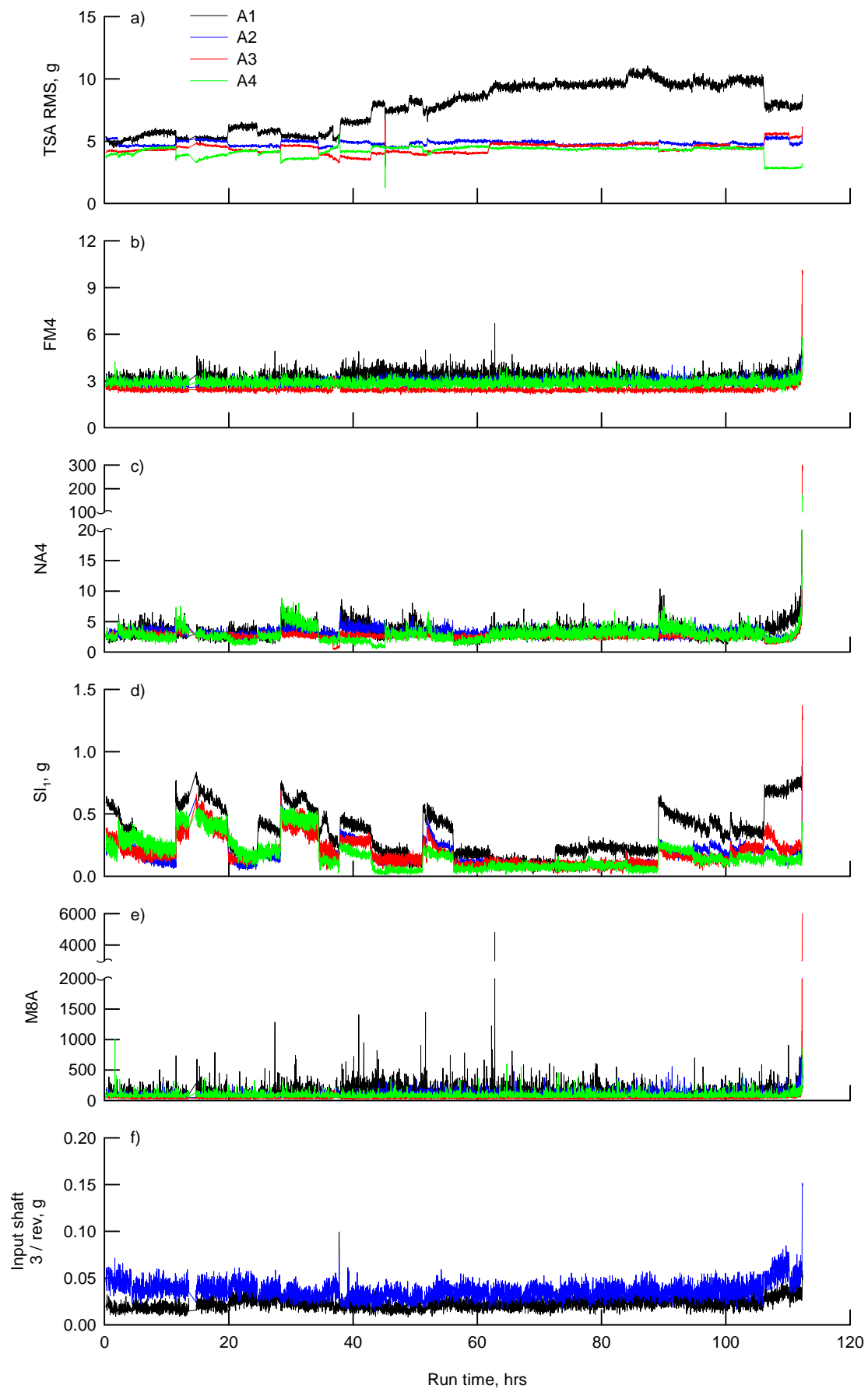
Fig. 15. MDSS fault detection condition indicators for entire test.
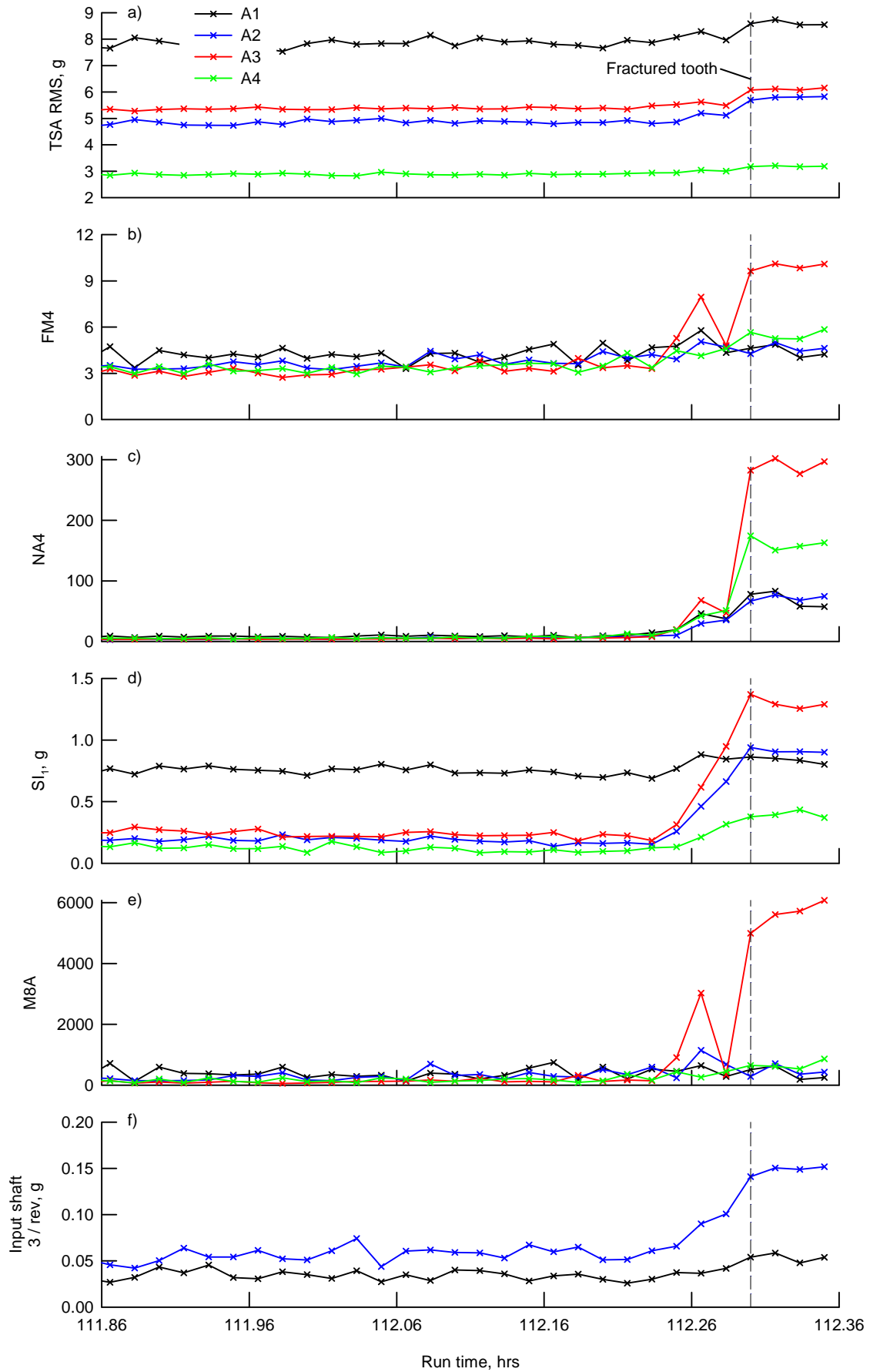
Fig. 16. MDSS fault detection condition indicators for last 30 minutes of test.
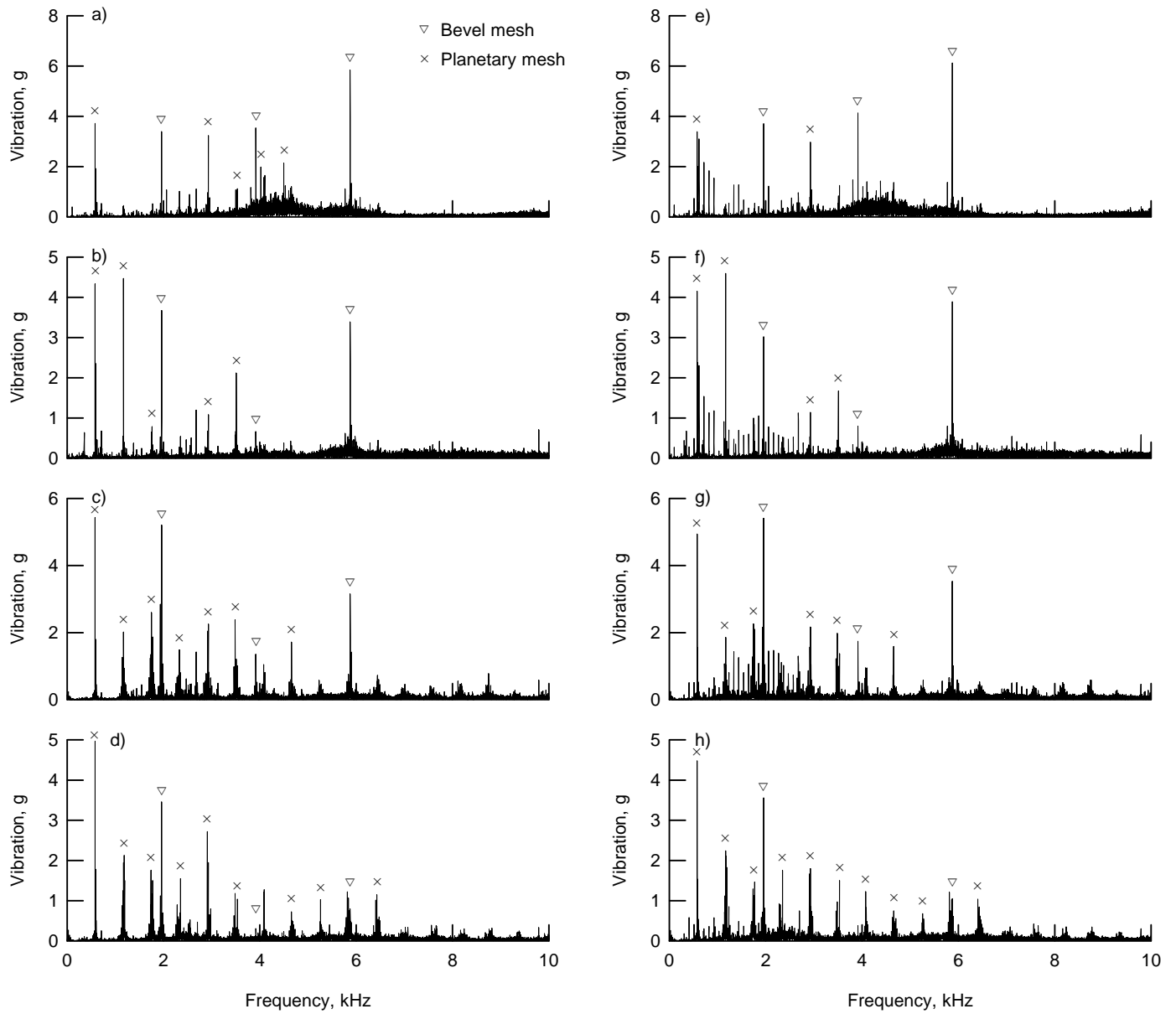
Fig. 17. MDSS sample spectrums. a) Accelerometer A1 at run time 110.50 hrs. b) Accelerometer A2 at run time 110.50 hrs. c) Accelerometer A3 at run time 110.50 hrs. d) Accelerometer A4 at run time 110.50 hrs. e) Accelerometer A1 at run time 112.35 hrs. f) Accelerometer A2 at run time 112.35 hrs. g) Accelerometer A3 at run time 112.35 hrs. h) Accelerometer A4 at run time 112.35 hrs.
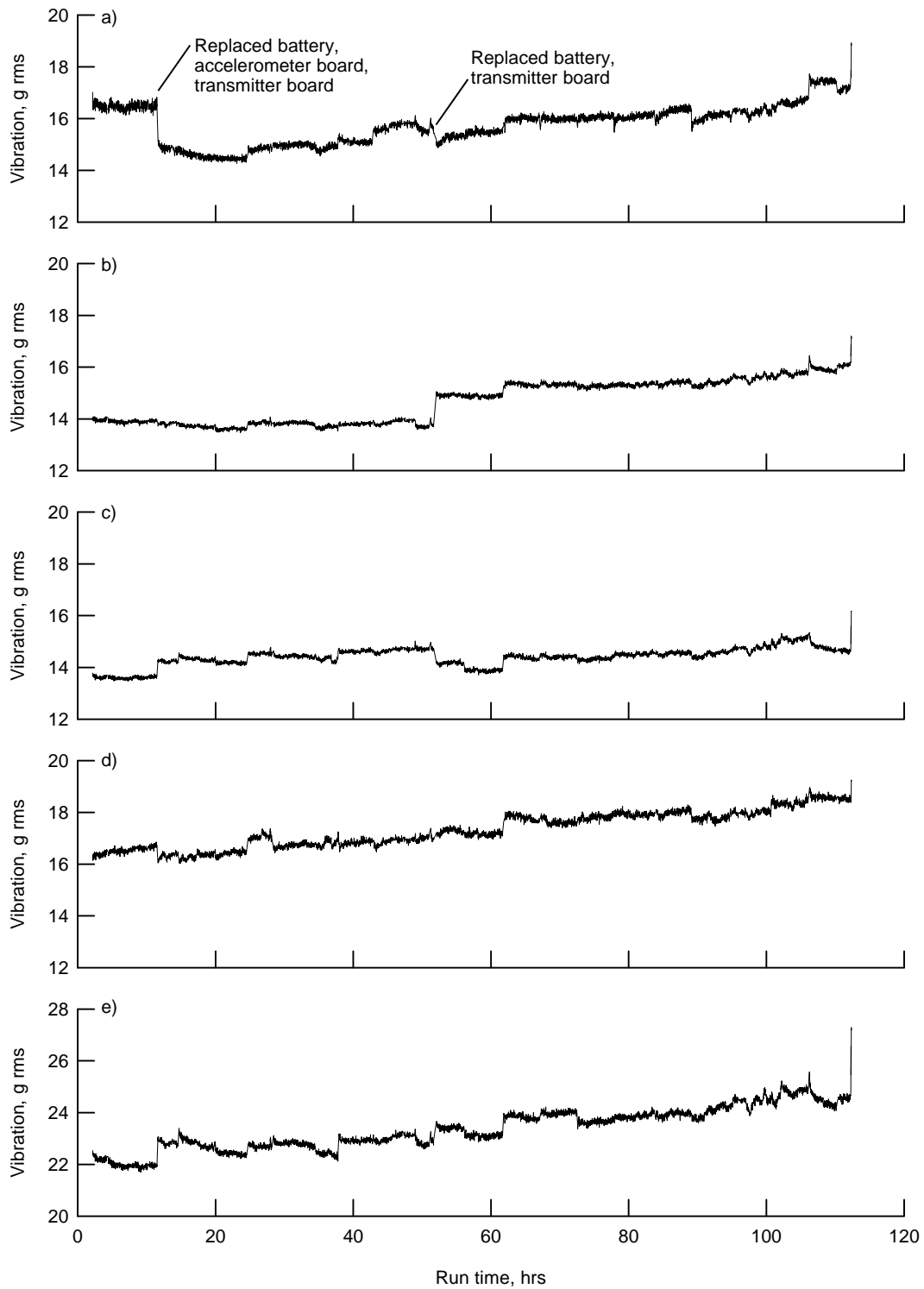
Fig. 18. RMS of MEMS raw vibration for entire test. a) Radial accelerometer, R. b) Tangential accelerometer, T1. c) Tangential accelerometer, T2. d) T1+T2, torsional acceleration. e) T1-T2, radial acceleration.
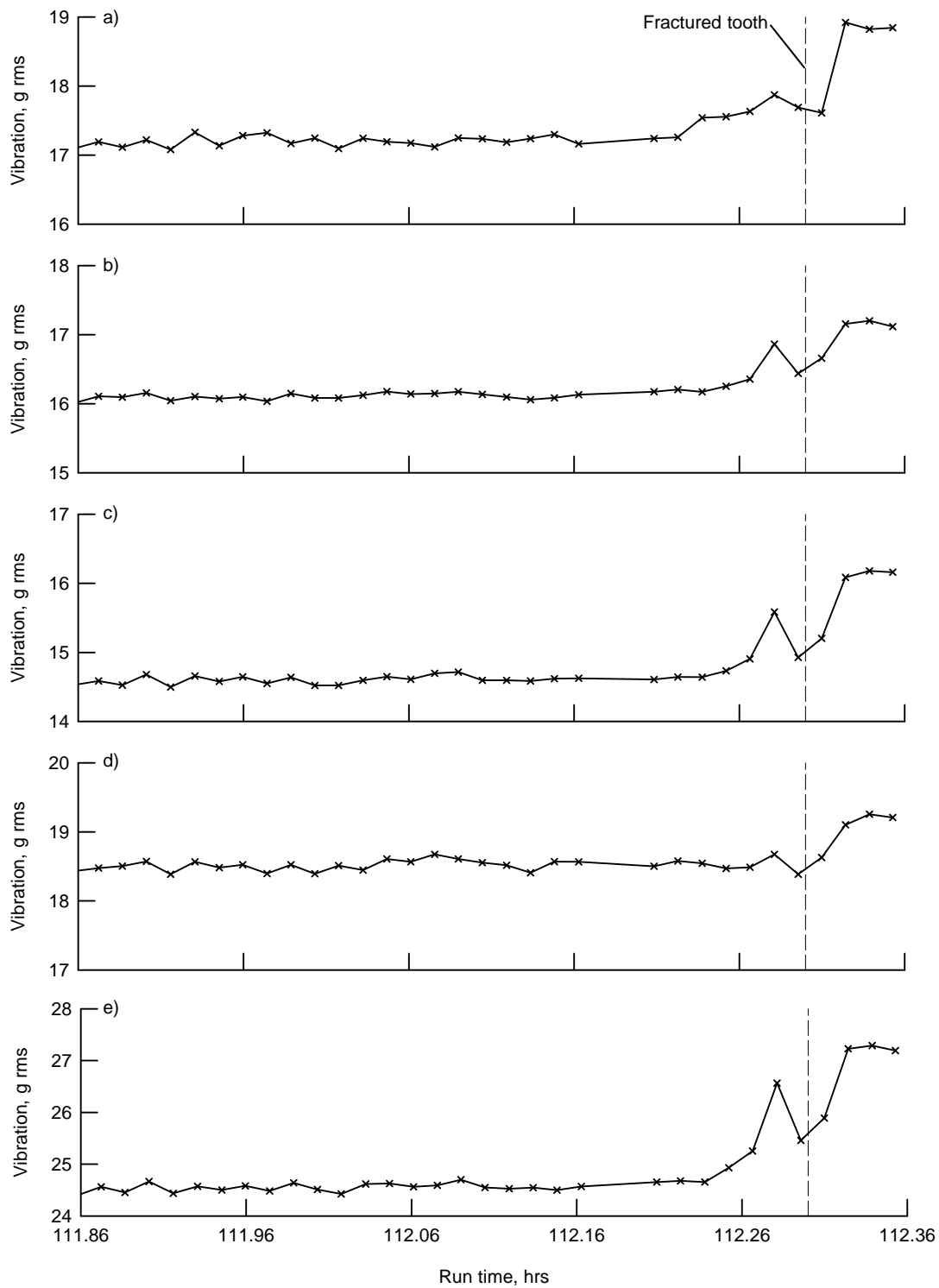
Fig. 19. RMS of MEMS raw vibration for last 30 minutes of test. a) Radial accelerometer, R. b) Tangential accelerometer, T1. c) Tangential accelerometer, T2. d) T1+T2, torsional acceleration. e) T1-T2, radial acceleration.
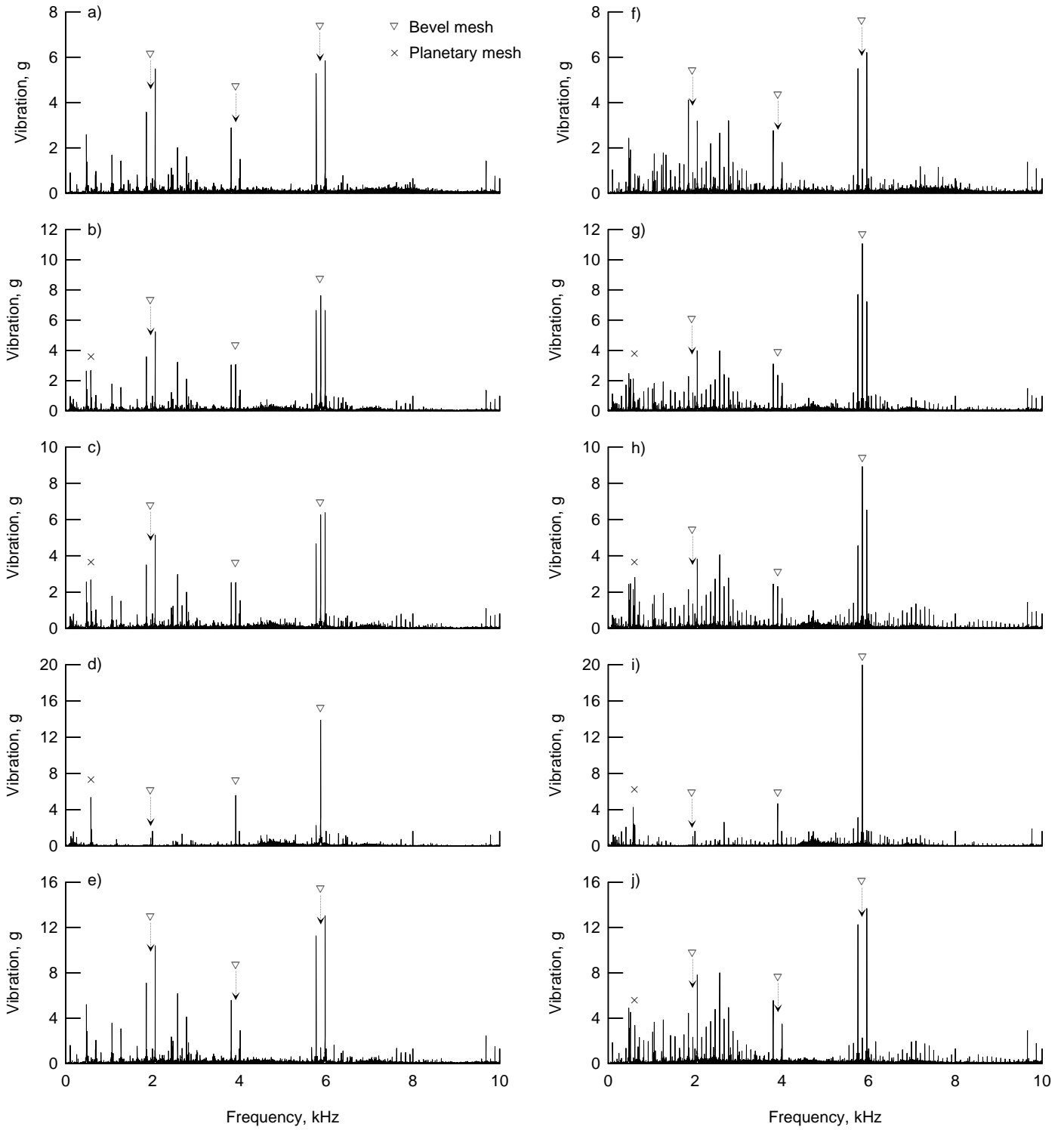
Fig. 20. MEMS sample spectrums. a) Radial accelerometer, R, at run time 110.49 hrs. b) Tangential accelerometer, T1, at run time 110.49 hrs. c) Tangential accelerometer, T2, at run time 110.49 hrs. d) T1+T2 at run time 110.49 hrs. e) T1-T2 at run time 110.49 hrs. f) R at run time 112.35 hrs. g) T1 at run time 112.35 hrs. h) T2 at run time 112.35 hrs. i) T1+T2 at run time 112.35 hrs. j) T1-T2 at run time 112.35 hrs.
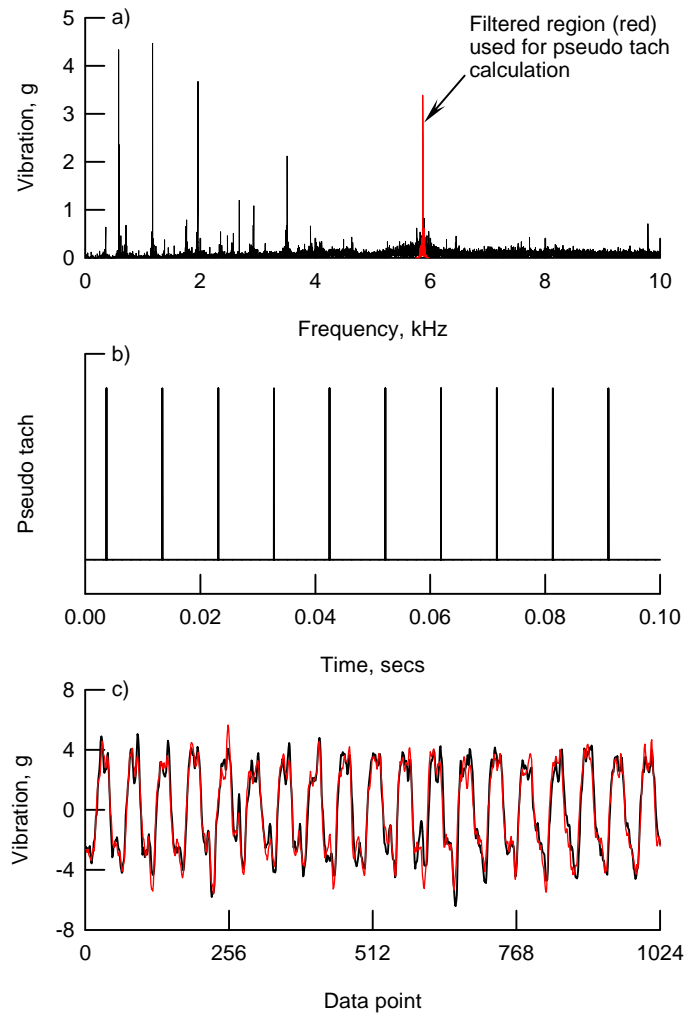
Fig. 21. Sample pseudo tach calculation results using MDSS data at run
time 110.50 hrs. a) Spectrum from accelerometer A2. b) Calculated
pseudo tach. c) Time synchronous averages (black: MDSS tach,
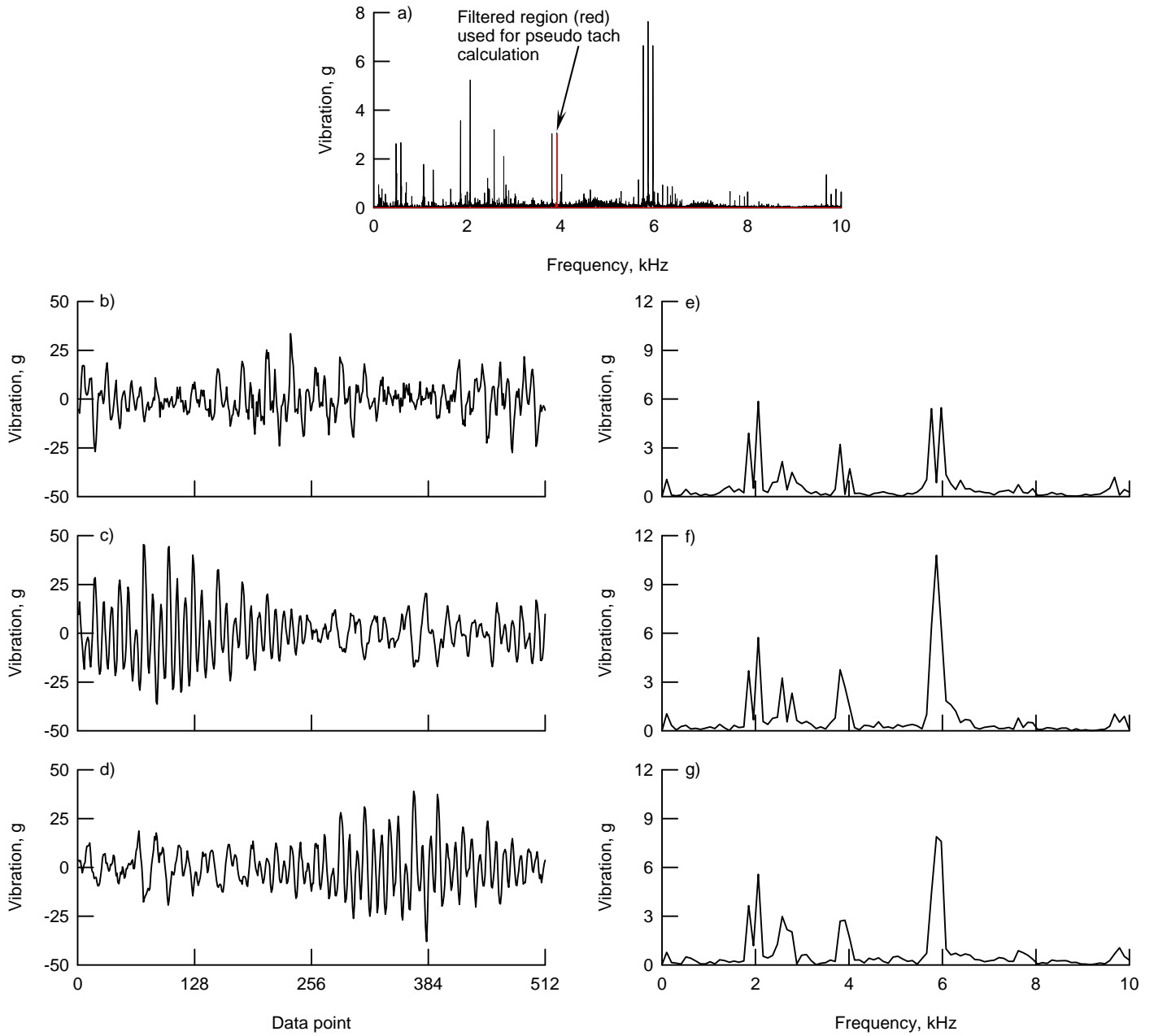red: Pseudo tach).

Fig. 22. Sample time synchronous average calculation results using MEMS data at run time 110.49 hrs. a) Spectrum from accelerometer T1, used for pseudo tach calculation. b) TSA, radial accelerometer, R. c) TSA, tangential accelerometer, T1. d) TSA, tangential accelerometer, T2. e) FFT of TSA, radial accelerometer, R. f) FFT of TSA, tangential accelerometer, T1. g) FFT of TSA, tangential accelerometer, T2.
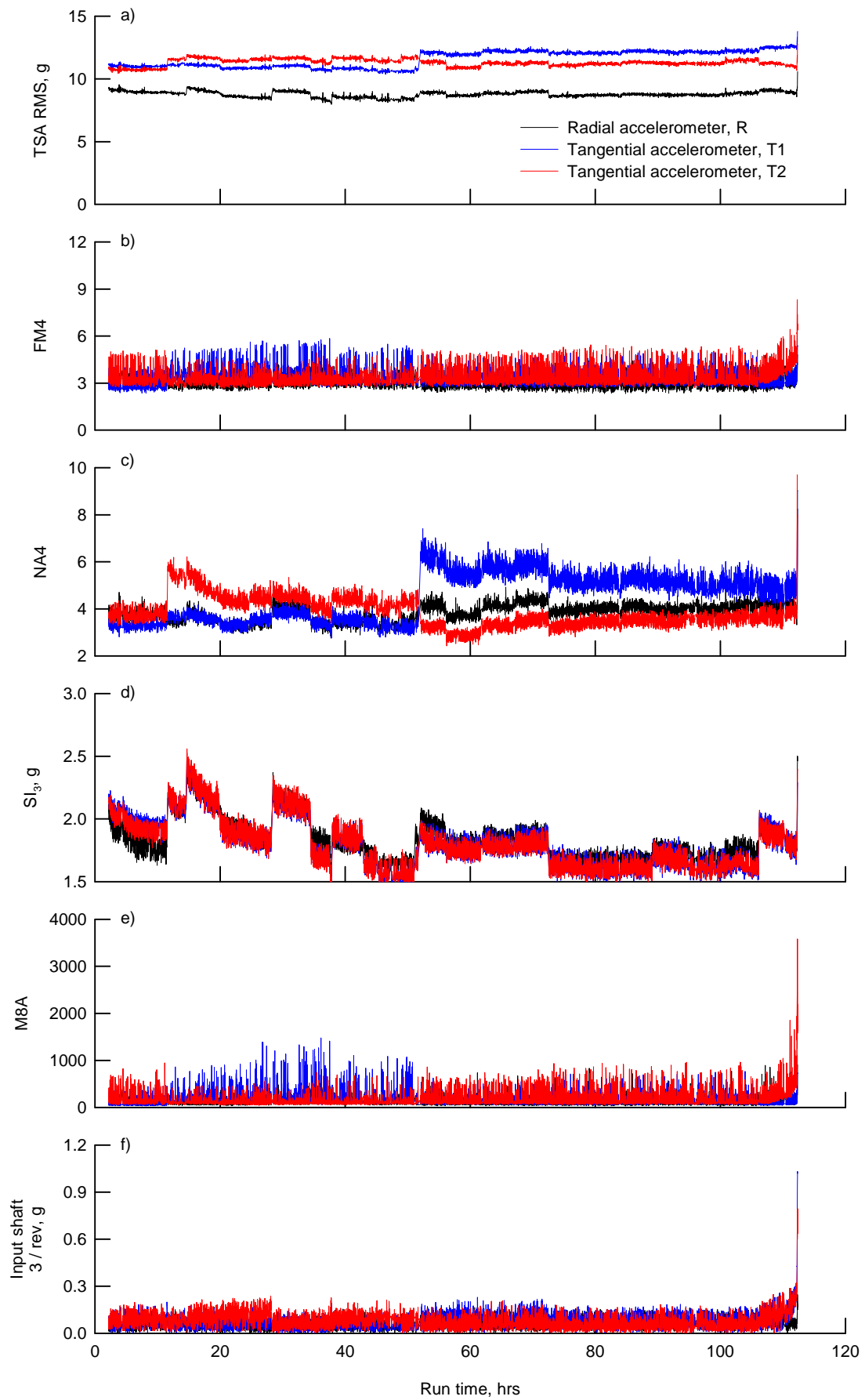
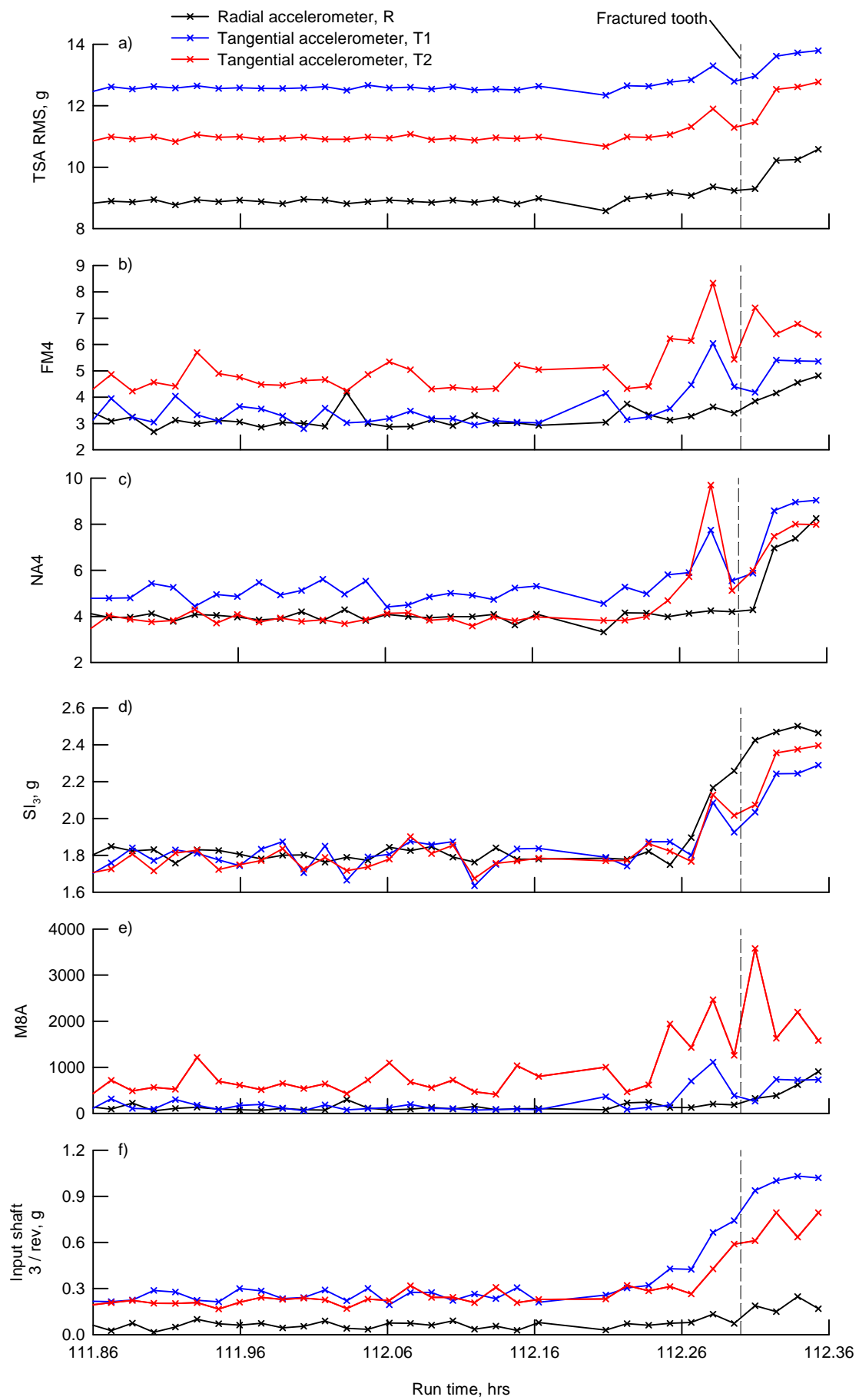Fig. 23. MEMS fault detection condition indicators for entire test.

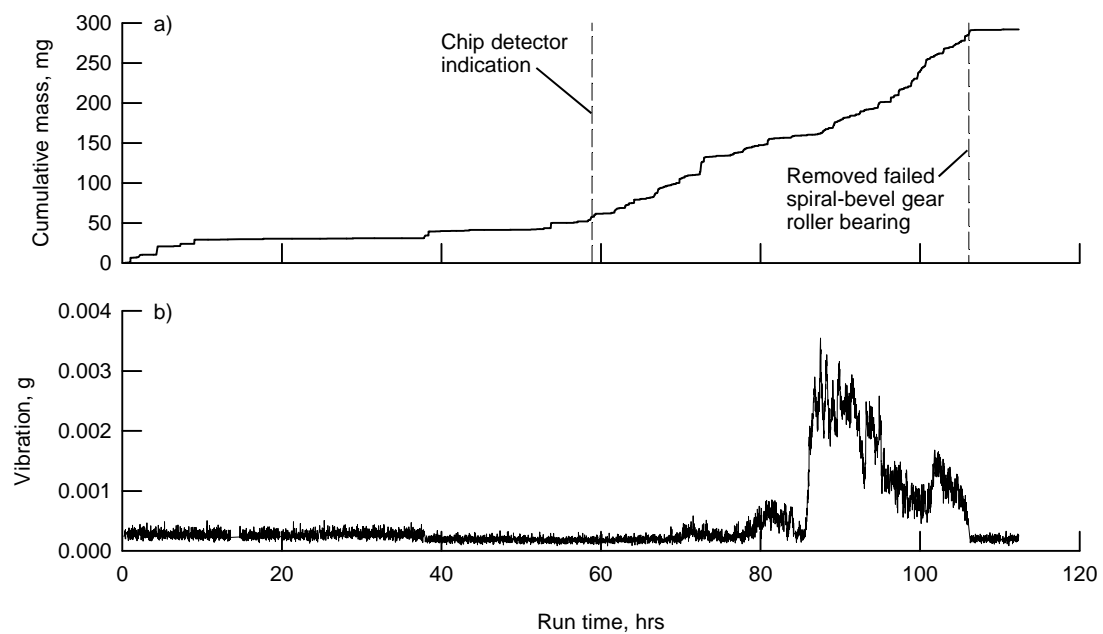Fig. 24. MEMS TSA condition indicators for last 30 minutes of test.

Fig. 25. Bearing fault detection condition indicators from MDSS data. a) Oil debris monitor
(ODM) cumulative mass. b) Accelerometer A3 bearing inner race condition indicator.